

# Invariants of the velocity-gradient, rate-of-strain, and rate-of-rotation tensors across the turbulent/nonturbulent interface in jets

Carlos B. da Silva<sup>a)</sup> and José C. F. Pereira

IDMEC/IST Technical University of Lisbon, Pav. Mecânica I, 1<sup>o</sup> andar/esq./LASEF,  
Av. Rovisco Pais, 1049-001 Lisboa, Portugal

(Received 14 August 2007; accepted 20 March 2008; published online 2 May 2008)

The invariants of the velocity gradient ( $R$  and  $Q$ ), rate-of-strain ( $R_S$  and  $Q_S$ ), and rate-of-rotation ( $Q_W$ ) tensors are analyzed across the turbulent/nonturbulent (T/NT) interface by using a direct numerical simulation (DNS) of a turbulent plane jet at  $Re_\lambda \approx 120$ . The invariants allow a detailed characterization of the dynamics, geometry and topology of the flow during the entrainment. The invariants  $Q$  and  $Q_S$  are almost equal and negative outside the turbulent region close to the T/NT interface, which shows the existence of high values of strain product (hence viscous dissipation of kinetic energy) at that location. Right at the T/NT interface, the invariants  $Q_W$  and  $Q_S$  show that virtually all flow points there are characterized by irrotational dissipation, with no discernible sign of the coherent structures which are known to exist deep inside the turbulent region. Moreover, the invariants of the velocity gradient tensor ( $Q$  and  $R$ ) show that the classical “teardrop” shape of their associated phase map is not yet formed at the T/NT interface. All the invariants rapidly change after the T/NT interface is crossed into the turbulent region. For instance, the enstrophy density, proportional to  $Q_W$ , is zero in the irrotational flow region and high and more or less constant inside the turbulent region, after it undergoes a sharp jump near the T/NT interface. Inside the turbulent region, at a distance of only  $1.7\eta$  from the T/NT interface, where  $\eta$  is the Kolmogorov microscale, the invariants  $Q_W$  and  $Q_S$  suggest that large scale coherent vortices already exist in the flow. Furthermore, the joint probability density function of  $Q$  and  $R$  already displays its well known teardrop shape at that location. Moreover, the geometry of the straining (or deformation) of the fluid elements during the turbulent entrainment process is preferentially characterized by biaxial expansion with  $\alpha_S:\beta_S:\gamma_S=2:1:-3$ , where  $\alpha_S$ ,  $\beta_S$ , and  $\gamma_S$  are the eigenvalues of the rate-of-strain tensor arranged in descending order. Based on an analysis of the invariants, many aspects of the flow topology inside the turbulent region at a distance of only  $1.7\eta$  from the T/NT interface are already similar to those observed deep inside the turbulent region. © 2008 American Institute of Physics. [DOI: 10.1063/1.2912513]

## I. INTRODUCTION

The study of the invariants of the velocity gradient, rate-of-strain, and rate-of-rotation tensors in turbulent flows has attracted much attention since the seminal papers by Chong *et al.*,<sup>1</sup> Cantwell,<sup>2,3</sup> and Perry and Chong.<sup>4</sup> The invariants are scalar quantities whose values are independent of the orientation of the coordinate system and contain information concerning the rates of vortex stretching and rotation, and on the topology and geometry of deformation of the infinitesimal fluid elements. Furthermore, the analysis of the invariants permits the understanding of these issues using a relatively small number of variables, e.g., the second and third invariants of the velocity gradient tensor combined ( $Q$  and  $R$ ) allow to assess the topology of the flow (enstrophy dominated versus strain dominated) or the enstrophy production (vortex stretching versus vortex compression).

The invariants have been extensively used in several flow configurations such as isotropic turbulence,<sup>5-7</sup> turbulent mixing layers,<sup>8</sup> and turbulent channel flows.<sup>9</sup> Important

information is also obtained by analyzing the volume integral of the invariants, as shown by Soria *et al.*<sup>10</sup> In these studies, several “universal” features of turbulent flows were observed. An example of such a result is the well known “teardrop” shape of the joint probability density function (PDF) of  $R$  and  $Q$ .

An interesting line of research using the invariants consists in writing transport equations for each one of the invariants.<sup>7</sup> Cantwell<sup>2</sup> analyzed these equations for the invariants of the velocity gradient tensor by using the so-called “restricted Euler model” proposed by Vieillefosse<sup>11</sup> where the pressure Hessian and viscous terms are neglected. The solutions to these equations showed some of the flow features observed in isotropic turbulence such as the preferred alignment of the vorticity vector with the eigenvector corresponding to the intermediate eigenvalue of the rate-of-strain tensor, as well as the tendency for a state corresponding to two positive and one negative eigenvalues of this tensor.<sup>12</sup>

Another line of active research involving the invariants has been the identification of the coherent structures in turbulent flows, either to visualize the flow regions associated with the presence of vortex tubes<sup>13-16</sup> or to identify the regions responsible for the most important dissipation rates of

<sup>a)</sup>Electronic mail: carlos.silva@ist.utl.pt.

kinetic energy.<sup>17,18</sup> Recently, the invariants have been used also in the context of subgrid-scale modeling.<sup>19,20</sup>

The present work uses the invariants in the context of the *turbulent entrainment* that exists in free shear flows such as mixing layers, wakes, and jets. In these flows, the flow field can be divided into two regions. In one region, the flow is turbulent (T) and its vorticity content is high, while in the other region, the flow consists of largely irrotational [nonturbulent (NT)] flow.<sup>21</sup> The two flow regions are divided by the turbulent/nonturbulent (T/NT) interface where the turbulent entrainment mechanism takes place, by which a given fluid element from the irrotational zone becomes turbulent. This T/NT interface is very sharp and is continually deformed over a wide range of scales. Its thickness is of the order of the Taylor microscale.<sup>22</sup>

The mechanism of turbulent entrainment is still involved in a great deal of mystery, despite the great number of works devoted to it (see, e.g., Townsend<sup>23</sup> for a review on the classical ideas of turbulent entrainment). Understanding of the physical mechanisms taking place at the T/NT interface is important in many natural and engineering flows since important exchanges of mass, momentum, and passive or active scalar quantities take place across the T/NT interface.<sup>24</sup> It was assumed in the past that the turbulent entrainment mechanism is mainly driven by “engulfing” motions caused by the large scale flow vortices,<sup>23</sup> but recent experimental and numerical works give more support to the original model of Corrsin and Kistler<sup>21</sup> where the entrainment is primarily associated with small scale (“nibbling”) eddy motions.<sup>25,26</sup> Nevertheless, it is still argued that the entrainment and mixing rates are largely determined by the large scales of motion.

Recently, the study of the turbulent entrainment saw very significant advances with the results from direct numerical simulations (DNSs) of plane wakes by Bisset *et al.*,<sup>27,28</sup> the DNSs of round jets by Mathew and Basu,<sup>25</sup> the experimental measurements of round jets by Westerweel *et al.*,<sup>26,29</sup> and with results from the flow generated by an oscillating grid by Holzner *et al.*<sup>30,31</sup> Many new and sometimes quite unexpected results were obtained in these works. One of the most surprising results (see Mathew and Basu<sup>25</sup> and Westerweel *et al.*<sup>26</sup>) consisted in the realization that the total amount of fluid entrained due to the small scale motions near the T/NT interface (i.e., nibbling) is more important than the amount of fluid entrained by large scale motions (engulfing), as suggested more than 50 years ago by Corrsin and Kistler.<sup>21</sup> Other interesting results are the existence of a finite jump in the tangential velocity (hence also in the  $|\Omega_z|$  vorticity component) at the T/NT interface<sup>26,28</sup> as anticipated by Reynolds,<sup>32</sup> the existence of a positive contribution to the enstrophy by the viscous enstrophy diffusion term,<sup>28,31</sup> the existence of a region of high strain product in the irrotational flow region close to the T/NT interface,<sup>31</sup> and the estimation of the characteristic scales of motion at the T/NT interface as being of the order of the Taylor scale.<sup>26</sup>

The goal of the present work is to analyze the evolution of the invariants of the velocity gradient, rate-of-strain, and rate-of-rotation tensors across the T/NT interface in turbulent jets in order to clarify the kinematics, dynamics, and topol-

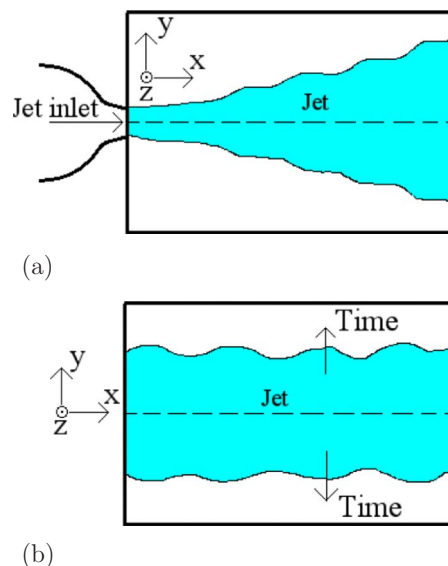


FIG. 1. (Color online) Sketch of (a) a spatially developing jet as produced in a laboratory setup and (b) a temporal jet simulation as the one adopted in the present work. Notice the coordinate system used in the present work indicating the streamwise ( $x$ ), normal ( $y$ ), and spanwise ( $z$ ) directions.

ogy of the flow during the entrainment process. For this purpose, a DNS of a turbulent plane jet will be used. The turbulent plane jet is a well known canonical free shear flow with many common features with other free shear flows such as mixing layers, wakes, round, and coaxial jets. Namely, the flow statistics are dominated by the presence of an inhomogeneous mean streamwise velocity profile and by the presence of quite similar long lived large scale flow vortices, originated from well known instabilities (e.g., Kelvin–Helmholtz instability), and whose “footprints” are still discernible at the far field fully developed turbulent state. Therefore, it is expected that the results obtained in the present study display some universal qualitative features related to the entrainment in free shear flows.

This article is organized as follows. In Sec. II, we describe the plane jet DNS used in the present work. Section III describes the procedure used to detect the T/NT interface and the data bank used in the subsequent analysis. The main results are described in Sec. IV. In Sec. V, the work ends with a review of the main results and conclusions.

## II. DNS OF TURBULENT PLANE JETS

### A. Statement of the problem

In this work, we are interested in analyzing the invariants of the velocity gradient, rate-of-strain, and rate-of-rotation tensors in connection with the mechanism of turbulent entrainment in jets. A typical spatially developing plane jet issuing from a nozzle into a tank filled with the same fluid, as obtained in a laboratory experiment, is sketched in Fig. 1(a). Recent DNS of spatially evolving turbulent plane jets include the works of Stanley *et al.*<sup>33</sup> and da Silva and Métais.<sup>34</sup>

It is well known that numerical simulations of spatially developing flows, i.e., *spatial simulations*, can be very de-

manding both in terms of computer time and memory due to the need to simulate the flow inside a very large computational domain containing all the length scales of the flow.

In the present work, a *temporal simulation* of a plane jet, as sketched in Fig. 1(b), was used in order to limit the computational cost. The sketch also shows the coordinate system used in the present work indicating the streamwise ( $x$ ), normal ( $y$ ), and spanwise ( $z$ ) directions. DNSs of temporally evolving turbulent plane jets were carried out by Akhavan *et al.*<sup>35</sup> and da Silva and Pereira.<sup>36</sup> In these simulations, the computational domain is periodic in the three spatial directions, which allows the use of very fast and accurate pseudospectral methods. Thus, one studies the temporal evolution of the flow generated by an initial plane jet velocity profile, instead of the flow of a spatially developing jet. This fact substantially limits the size of the computational domain required by the simulations, which reduces the computational cost.

Because in temporal simulations periodic boundary conditions are used in the streamwise direction, the feedback effects caused by the pressure field that are known to influence the details of the transition to turbulence (e.g., see Thomas and Chu<sup>37</sup>) are absent from temporal simulations. Another drawback of temporal simulations is that no rigorous comparison with experimental results can be made. However, since the flow field in the fully developed turbulent state is to a great extent independent of the details of the transition to turbulence (e.g., see Refs. 33–36), temporal simulations are a useful tool to analyze the flow at the far field of a turbulent jet. Also, the large scale flow structures that are typical of jets and other free shear flows, such as the Kelvin–Helmholtz and streamwise vortices, are well captured in temporal simulations. The use of temporal simulations is also justified by the fact that despite their limitations, they represent valid solutions to the Navier–Stokes equations and are relevant since the goal of the present work is to analyze those features of the entrainment mechanism that are generally true in Navier–Stokes turbulence. Another justification comes from the fact that turbulent entrainment is mainly dominated by small scales, as shown by Mathew and Basu<sup>25</sup> and Westerweel *et al.*<sup>26,29</sup> Temporal DNSs of turbulent flows were previously used to analyze the mechanics of the T/NT interface in plane wakes<sup>27,28</sup> and in round jets.<sup>25,38</sup>

## B. Numerical method

The numerical code used here is a standard pseudospectral code (collocation method<sup>39</sup>) in which the temporal advancement is made with an explicit third order Runge–Kutta time stepping scheme.<sup>40</sup> The simulation was fully dealiased by using the  $\frac{3}{2}$  rule.<sup>39</sup> This code was used recently by the authors in DNSs of turbulent plane jets described in da Silva and Pereira.<sup>36</sup>

## C. Physical and computational parameters

The DNS was started by using, as initial condition, an hyperbolic-tangent velocity profile,

$$U(x, y, z) = \frac{U_1 + U_2}{2} - \frac{U_1 - U_2}{2} \tanh \left[ \frac{H}{4\theta_0} \left( 1 - \frac{2|y|}{H} \right) \right], \quad (1)$$

where  $\theta_0$  is the initial momentum thickness,  $H$  is the inlet nozzle of the jet, and we used  $U_1=1$  and  $U_2=0$ . The mean profile defined by Eq. (1) was also used as the inlet condition in the spatial plane jet simulations of Stanley *et al.*<sup>33</sup> and Silva and Métais<sup>34</sup> and as the initial condition in the temporal simulations of Akhavan *et al.*<sup>35</sup> and da Silva and Pereira.<sup>36</sup> Many spatial and temporal simulations of turbulent round jets use similar (inlet or initial) mean velocity profiles (see, e.g., da Silva and Métais<sup>41</sup> and Mathew and Basu<sup>25</sup>) since it is recognized that it represents a very good approximation to the inlet velocity profile found in measured experimental jets.<sup>42</sup>

A three-component velocity fluctuating “spectral noise” was superimposed to the mean velocity profile defined by Eq. (1) through a proper convolution function that imposes the velocity fluctuations in the initial shear layer region of the jet. The spectral noise used here is very similar to the one used in da Silva and Métais<sup>34</sup> and virtually equal to the one used in da Silva and Pereira.<sup>36</sup> This numerical noise is very similar to the standard noise used to initialize simulations of decaying isotropic turbulence (e.g., Lesieur *et al.*<sup>43</sup>). In short, each velocity component of the noise is prescribed in such a way that its energy spectrum is given by  $E(k) \sim k^s \exp[-s/2(k/k_0)^2]$ , where the exponent  $s$  is  $s \leq 4$  (as in decaying isotropic turbulence). However, here, the peak wave number  $k_0$  is chosen to give an energy input which is dominant at small scales (high  $k_0$ ) to allow the simulation to evolve “naturally” by “selecting” its natural instability modes.

As in Stanley *et al.*,<sup>33</sup> da Silva and Métais,<sup>34</sup> and da Silva and Pereira,<sup>36</sup> a relatively high amplitude spectral noise was added (8%) to the mean profile defined by Eq. (1) in order to speed up the transition mechanism and allow the flow to quickly reach a fully developed turbulent state. It is important to stress that, as shown in previous works, the addition of a high  $H/\theta_0$  ratio and initial amplitude noise, although favoring a faster transition to turbulence, does not affect the dynamics of the self-similar fully developed turbulent state.<sup>33,34,36,44</sup>

In the present work, we are interested in reaching a slightly higher Reynolds number than in Ref. 36 and at the same time in having a resolution closer to the one used in isotropic turbulence, for which the optimal value is  $\Delta x/\eta \approx 2.1$  (Pope<sup>45</sup>) and which corresponds to having  $k_{\max}\eta=1.5$ , where  $k_{\max}$  is the maximum resolved wave number and  $\eta$  is the Kolmogorov microscale. For this purpose in the present plane jet simulation, we use an initial Reynolds number equal to  $Re_H=(U_1-U_2)H/\nu=3200$ ,<sup>46</sup> where  $H$  is the plane jet inlet slot width, and we reduce the extent of the computational box to  $(L_x, L_y, L_z)=(4H, 6H, 4H)$ . The grid consists now in  $(N_x \times N_y \times N_z)=(256 \times 384 \times 256)$  grid points, i.e., the number of grid points along the streamwise ( $x$ ) and normal ( $y$ ) directions was retained from Ref. 36, while the spanwise ( $z$ ) resolution was doubled. This was done in order

to improve the degree of convergence of the statistics over one single instantaneous field. Notice, however, that the grid remains isotropic and we have  $\Delta x = \Delta y = \Delta z = 0.0156H$  instead of  $0.02H$  as in Ref. 36. Finally, in order to further reduce the time spent during the transition phase, the initial  $H/\theta_0$  ratio was raised to  $H/\theta_0 = 35$ .

It is important to ensure that the new computational box size does not constrain the jet in its development and particularly its spreading rate. Recall that the use of classical pseudospectral schemes for spatial discretization implies that the boundary conditions used here are periodic in the three spatial directions. Concerning the box size in the streamwise direction, it is important to ensure that the size of the computational domain in this direction is big enough to allow for the development of the primary (shear layer) Kelvin–Helmholtz instability. Therefore, the box size has to be greater than the Kelvin–Helmholtz instability length scale. The Strouhal number of the primary Kelvin–Helmholtz instability is equal to  $S_{sl} = f_{sl}\theta_0/U_C = 0.033$ , where  $f_{sl}$  is the frequency of the shear layer mode and  $U_C = 0.5(U_1 + U_2)$  is the convection velocity.<sup>47</sup> Since the initial  $H/\theta_0$  ratio used here is  $H/\theta_0 = 35$ , the associated instability length scale is equal to  $\lambda_{sl} = \theta_0/S_{sl} = 0.87H$ . Thus, the box size in the streamwise direction  $L_x = 4H$  is more than four times bigger than the Kelvin–Helmholtz instability length scale.

Concerning the normal direction, it is important to emphasize that numerous previous works have showed that there is no particular problem with the use of periodic boundary conditions provided that the box size is big enough (see da Silva and Métais<sup>34</sup> and Mathew and Basu<sup>25</sup> and references therein). The box size along the normal direction used here is  $L_y = 6H$ . This is the same lateral size used in the simulations of Mathew and Basu.<sup>25</sup> As shown in numerous visualizations, including the one shown below in Fig. 5, the contours that delimit the T/NT interface are on average at a distance of more than  $1.5H$  from the normal box boundaries. This is more than the distance used in previous numerical simulations used to analyze the turbulent entrainment, e.g., Mathew and Basu<sup>25</sup> had less than  $1D$  ( $D$  is the jet diameter), and this still posed no problems. Moreover, all the one point statistics obtained in the present simulation are in excellent agreement with the results from previous experimental and numerical works (see below). Thus, the lateral extent or boundary conditions in the normal direction do not influence the plane jet development. Finally, concerning the box size in the spanwise direction, we now have  $L_z = 4H$ . This is larger than any of the spanwise box sizes used in the spatial or temporal simulations cited above, and since the length scales, of the secondary (spanwise) instabilities are smaller than the primary instabilities (estimated above as  $\lambda_{sl} = 0.87H$ ), with  $L_z = 4H$ , the box size used in the present simulation is indeed sufficient.

#### D. DNS assessment

The scenario of transition to turbulence is very similar to the one described in previous numerical simulations, e.g., Stanley *et al.*<sup>33</sup> da Silva and Métais,<sup>34</sup> and da Silva and Pereira,<sup>36</sup> and is characterized by the emergence of Kelvin–

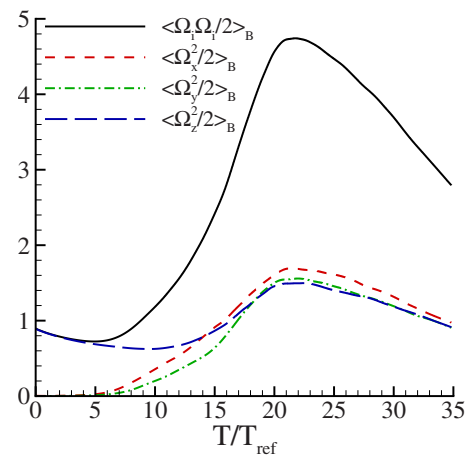


FIG. 2. (Color online) Temporal evolution of the mean enstrophy and its components for the present turbulent plane jet DNS.

Helmholtz vortices, both at the upper and lower shear layers, and is followed by the appearance of pairs of streamwise vortices connecting each two consecutive pairs of Kelvin–Helmholtz rollers. Shortly after, the streamwise vortices break up into smaller structures with no preferential direction, which is a sign of a fully developed turbulent stage.

Figure 2 shows the temporal evolution of the enstrophy and its components averaged over the whole computational domain. We denote these averages by  $\langle \rangle_B$ , e.g.,

$$\left\langle \frac{\Omega_x^2(t)}{2} \right\rangle_B = \frac{1}{N_x N_y N_z} \sum_{i=1}^{N_x} \sum_{j=1}^{N_y} \sum_{k=1}^{N_z} \frac{\Omega_x^2}{2}(x, y, z, t). \quad (2)$$

As in Ref. 36, these curves show an increase until  $T/T_{ref} \approx 20$ , where  $T_{ref} = H/[2(U_1 - U_2)]$ , followed by a decrease at a more or less constant rate.

The coherent structures of the flow were visualized by using the “ $Q$  criteria”<sup>13,14</sup> and the pressure field. From  $T/T_{ref} \approx 15$  onward these structures are qualitatively similar to the ones shown in Figs. 2(a) and 2(b) from Ref. 36, i.e., the small scale structures, which are more easily visualized through positive values of  $Q$ , do not show the existence of any particular spatial orientation, whereas the low pressure isosurfaces, which highlight the bigger structures, still show remnants of the Kelvin–Helmholtz rollers (as in Ref. 36, there is, of course, some overlap between the structures from the two visualization criteria—see Dubief and Delcayre<sup>15</sup>). The self-similar regime is obtained at  $T/T_{ref} \approx 20$  (against  $T/T_{ref} \approx 30$  in Ref. 36), which corresponds to an equivalent streamwise location of  $x/H = (U_1 - U_2)(T/H) = T/(2T_{ref}) = 10$ . Recall that in the spatial simulations of Stanley *et al.*<sup>33</sup> and da Silva and Métais,<sup>34</sup>  $x/H = 10$  marked also the beginning of the self-similar regime. Finally, at this station, the Reynolds number based on the Taylor microscale  $\lambda$  and on the root mean square of the streamwise velocity  $u'$  is equal to  $Re_\lambda = u'\lambda/\nu \approx 120$  across the shear layer.

Figures 3(a)–3(d) show one point statistics for the plane jet DNS. The statistics were obtained with a single instantaneous field from the self-similar region where spatial averaging in the two homogeneous directions ( $x$  and  $z$ ) was followed by “folding” of the mean profiles in relation to the jet

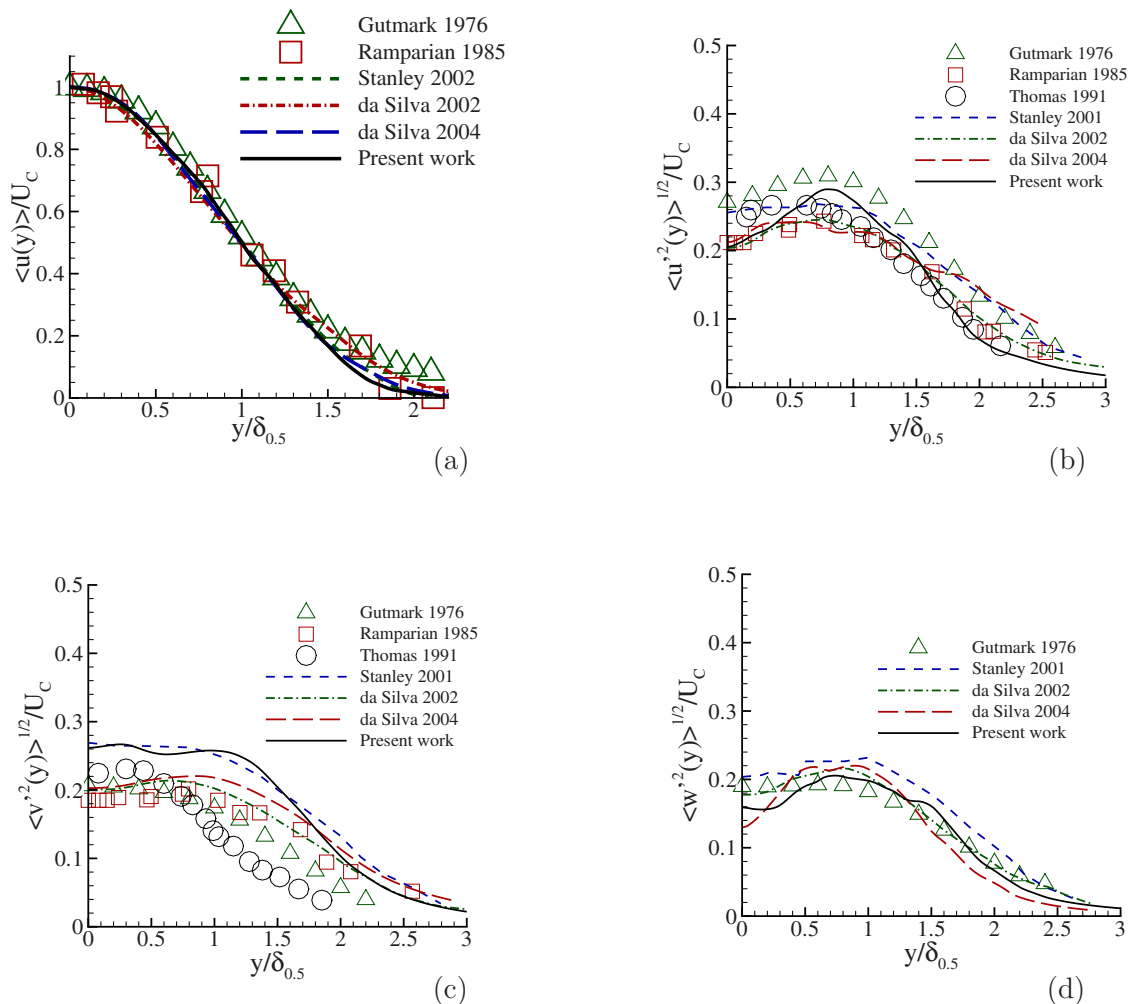


FIG. 3. (Color online) Profiles of several one point statistics at the self-similar region from the present temporal plane jet direct numerical simulation (present work) compared to the experimental results from Gutmark and Wynagnsky (Ref. 50), Ramparian and Chandrasekhara (Ref. 51), and Thomas and Prakash (Ref. 52) and with the DNSs of Stanley *et al.* (Ref. 33), da Silva and Métais (Ref. 34), and da Silva and Pereira (Ref. 36): (a) Mean streamwise velocity, (b) streamwise Reynolds stresses, (c) normal Reynolds stresses, and (d) spanwise Reynolds stresses.  $U_c$  is the streamwise mean centerline velocity and  $\delta_{0.5}$  is the half-width of the jet.

centerline ( $y=0$ ) to take advantage of the symmetry of the jet. We denote these averages by  $\langle \rangle$ ,

$$\langle u(y) \rangle = \langle u(y, t) \rangle = \frac{1}{N_x N_z} \sum_{i=1}^{N_x} \sum_{k=1}^{N_z} \frac{1}{2} [u(x, y, z, t) + u(x, -y, z, t)]. \quad (3)$$

Due to the relatively small number of samples obtained for each  $y$  coordinate ( $2N_x \times N_z = 131\,072$ ), the mean profiles show some wiggles. This limitation is a well known feature of temporal simulations and similar wiggles can be found also in the mean profiles from temporal simulations of mixing layers,<sup>48</sup> wakes,<sup>49</sup> and round jets.<sup>50</sup> Although the degree of convergence of the statistics is not perfect, they nevertheless allow a comparison to results from experimental and numerical works from the literature. In Figs. 3(a)–3(d), the present results are compared to experimental results from Gutmark and Wynagnsky,<sup>50</sup> Ramparian and Chandrasekhara,<sup>51</sup> and Thomas and Prakash,<sup>52</sup> and the DNSs, from Stanley *et al.*,<sup>33</sup> da Silva and Métais,<sup>34</sup> and

da Silva and Pereira.<sup>36</sup> Although the scatter between the experiments and computations is high, the mean streamwise velocity profile and Reynolds stress profiles from the present DNS agree with the data available well.

Figures 4(a) and 4(b) show the spatial three-dimensional kinetic energy and kinetic energy dissipation spectra, respectively, at several instants. The kinetic energy spectrum has a  $-5/3$  region followed by a smooth decay at high wave numbers. Notice that the product of the maximum resolved wave number to the Kolmogorov microscale is  $k_{\max} \eta \approx 1.5$ . That the dissipative scales are indeed being well resolved is attested by the small upturns at the end of the wave number range. The dissipation spectrum shown in Fig. 4(b) peaks at  $k\eta \approx 0.3$ , which marks the start of the dissipation region. The shape and magnitudes of these spectra are very similar to the ones obtained by Akhavan *et al.*,<sup>35</sup> also in temporal simulations of turbulent plane jets, with similar resolution and similar Reynolds number based on the Taylor microscale. Additional resolution tests are given in Appendix A.

These results show that the present DNS is both accu-

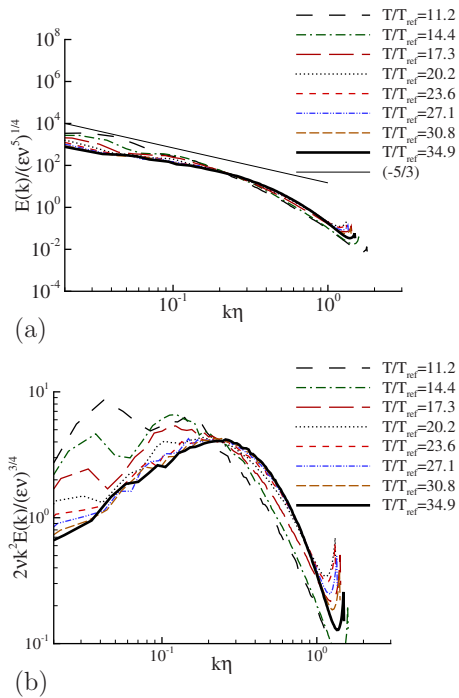


FIG. 4. (Color online) Three-dimensional (spatial) kinetic energy and kinetic energy dissipation spectra from the plane jet DNS at several instants: (a) Kinetic energy spectrum and (b) kinetic energy dissipation spectrum.

rate, at the large and small scales, and representative of a fully developed turbulent plane jet. This completes the validation of the turbulent plane jet DNS.

### III. DATA BANK DESCRIPTION

#### A. Detection algorithm for the T/NT interface

The T/NT interface can be defined by using either the vorticity norm  $\Omega = (\Omega_i \Omega_i)^{1/2}$ , where  $\Omega_i$  is the vorticity field as in Bisset *et al.*,<sup>27,28</sup> or using a passive scalar or concentration field as in Westerweel *et al.*<sup>26,29</sup> The vorticity norm was used in the present work, where it was observed that the detection threshold of  $\Omega = 0.7U_1/H$  best delineated the vortical regions. This is exactly the same value used by Bisset *et al.*<sup>28</sup> and a similar level was used by Mathew and Basu.<sup>25</sup> Figure 5 shows contours of vorticity modulus corresponding to this detection threshold in an  $(x, y)$  plane of the jet at  $T/T_{ref} = 27$ . As in previous works, it can be seen that the T/NT interface is strongly contorted and some irrotational fluid is engulfed.

In the present work, we analyze conditional statistics in relation to the location of the interface envelope by using a procedure similar to the one described in previous works, e.g., Bisset *et al.*<sup>27,28</sup> and Westerweel *et al.*<sup>26,29</sup>

A detailed description of this procedure is given here with the aid of a sketch shown in Fig. 6. The sketch represents the T/NT interface separating the T from the irrotational or NT flow regions, at the upper shear layer of the plane jet. The vorticity surface defined by the selected threshold is indicated by a solid line, while the T/NT interface envelope is represented by gray dashed lines. The sketch depicts events of large scale engulfment and small scale nibbling

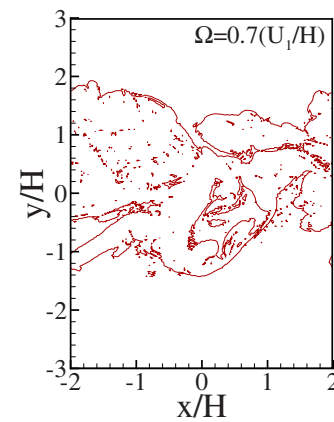


FIG. 5. (Color online) Contours of vorticity modulus corresponding to  $\Omega = 0.7U_1/H$  in the  $(x, y)$  plane of the jet at  $T/T_{ref} = 27$ .

and also the original coordinate system  $(x, y)$  used in the numerical simulation of the turbulent plane jet.

Since the plane jet is homogeneous in the streamwise  $(x)$  and spanwise  $(z)$  directions, each  $(x, y)$  plane is independently treated. Consider the upper shear layer depicted in Fig. 6. The procedure starts with the determination of the T/NT interface envelope location  $Y_I(x)$ , for each one of the  $N_x$  grid points in the original coordinate system along the  $x$  direction.  $Y_I(x)$  is obtained through a linear interpolation along the  $y$  direction, using the vorticity norm threshold indicated above to detect the T/NT interface.

In order to make conditional statistics in relation to the location of the interface envelope, we start by defining a new local coordinate system  $(x_I, y_I)$  with the lines tangent ( $x_I$ ) and normal ( $y_I$ ), respectively, to the interface envelope (see Fig. 6). In this new coordinate system, the T/NT interface is exactly at  $(x_I, y_I) = (0, 0)$ .

After the determination of the interface envelope  $Y_I(x)$ , one determines the coordinates of the axis line  $y_I$ , from the new (local) coordinate system  $(x_I, y_I)$ , in the old coordinate system  $(x, y)$ . Notice that this line is normal to the envelope for each one of the  $N_x$  grid points along the  $x$  direction. Along both sides of this  $y_I$  axis line (for  $y_I > 0$  and  $y_I < 0$ ), we define  $N_I = 80$  points, starting at  $y_I = 0$  and equally spaced

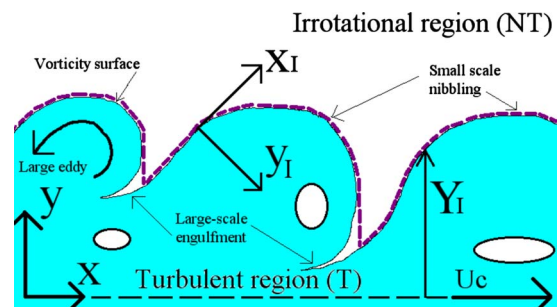


FIG. 6. (Color online) Sketch of the T/NT interface for the plane jet indicating the vorticity surface (solid line) and the interface envelope (gray dashed lines). The sketch also shows the coordinate system used in the computation of the plane jet  $(x, y)$  and the one used to analyze the T/NT interface  $(x_I, y_I)$ . In particular, the coordinate of the interface envelope is denoted by  $Y_I$ . The three holes represent regions of irrotational fluid inside the turbulent region.

with a distance equal to the mesh spacing  $\Delta x$ . For instance, the coordinates of these points in the turbulent region are given by  $(x_l, y_l) = [0, y_l(l)] = [0, (l-1)\Delta x]$  with  $l=1, N_l$ . This defines a total of  $2 \times N_l - 1 = 159$  grid coordinates for the axis  $y_l$ , which will be used to describe the mean conditional statistical profiles. Then, for each coordinate  $y_l$ , the mean conditional profile of a given flow variable  $P(x, y, z, t)$ , in the upper shear layer, for the plane  $(x, y)$  corresponding to  $z=Z$  and at time  $t=T$  is obtained through

$$\langle P(y_l) \rangle_I^{Up} = \frac{1}{N_L} \sum_{N_L} \bar{P}^{y_l}(x, y, z=Z, t=T), \quad (4)$$

where  $\bar{P}^{y_l}(x, y, z=Z, t=T)$  is the value of  $P(x, y, z, t)$  interpolated into the point  $(x_l, y_l) = (0, y_l)$  in the plane  $(x, y, z=Z)$  and at time  $t=T$ . A simple bilinear interpolation is used for this purpose.  $N_L$  is the total number of samples used to make the conditional mean for a given coordinate  $y_l$ . The maximum possible value for  $N_L$  is  $N_L = N_x$ ; however, during the computation of the mean conditional profile defined in Eq. (4), all points inside “holes” of “ambient fluid” that appear in the jet, such as the three holes represented in Fig. 6, are removed from the statistical sample.

The procedure just described is also used for the lower shear layer and the resulting profiles are averaged in the end. Thus, the maximum number of samples used to make a conditional mean for a given coordinate point  $y_l$  in a given  $(x, y)$  plane is then equal to  $2 \times N_x$ . The same procedure is used for each one of the  $(x, y)$  planes available and the final result is once again averaged over all the existing  $N_z$  planes. The maximum possible number of samples corresponding to a single instantaneous field is then equal to  $2 \times N_x \times N_z = 131\,072$ .

Finally, to further improve the degree of convergence of the conditional statistics, several instantaneous fields taken from the fully developed turbulent regime were also used. Although the plane jet evolves in time and thus each instantaneous field is, in its details, different from the others, selecting fields separated by a very small time interval reduces these differences. In particular, in the far field, self-similar, fully developed turbulent regime, each instantaneous field is statistically equivalent. Here, we used  $N_T = 11$  instantaneous fields taken from  $T/T_{\text{ref}} = 20.2$  to  $T/T_{\text{ref}} = 27.0$ . As can be seen in the kinetic energy and kinetic energy dissipation spectra shown in Figs. 4(a) and 4(b), there are no appreciable differences concerning these statistics for all the instantaneous fields from  $T/T_{\text{ref}} = 20.2$  to  $T/T_{\text{ref}} = 27.0$ , a fact confirmed by comparing the visualization of the fields from  $T/T_{\text{ref}} = 20.2$  and  $T/T_{\text{ref}} = 27.0$ . Thus, the use of these  $N_T$  instantaneous fields from the self-similar regime allows us to increase the total number of samples used in the conditional averages without “mixing” different regimes of the plane jet development.

Therefore, except for the data points which are removed from the averaging procedure for being part of holes of irrotational fluid in the turbulent zone (and likewise for being islands of turbulent fluid in the irrotational zone), the total number of samples used to make a conditional mean in relation to the distance from the T/NT interface is equal to

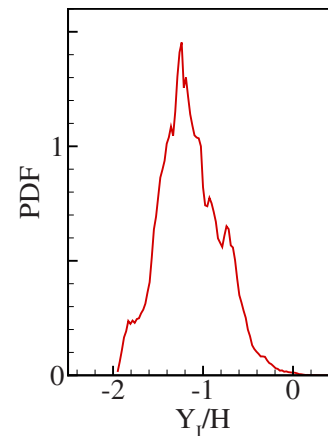


FIG. 7. (Color online) PDF of the vertical distance of the T/NT interface  $Y_I$  for the lower shear layer.

$\approx 2 \times N_T \times N_x \times N_z \approx 1.4 \times 10^6$ . This is more than enough to obtain well converged statistics of the quantities in study in this work.

With this procedure, conditional statistics of any flow quantity can be made in relation to the distance from the T/NT interface. We denote these conditional interface statistics by  $\langle \rangle_I$  to differentiate them from the spatial statistics done along the homogeneous directions of the plane jet, which are denoted by  $\langle \rangle$ , and from the spatial statistics done in the whole computational box, which we denote by  $\langle \rangle_B$ .

Figure 7 shows the PDF of the interface distance from the center of the jet  $Y_I$  for the lower shear layer (nondimensionalized by  $H$ ). The mean, variance, skewness, and flatness of the interface distance are  $\langle Y_I/H \rangle = -1.14$ ,  $\langle (Y_I/H)^2 \rangle = 0.12$ ,  $\langle (Y_I/H)^3 \rangle / \langle (Y_I/H)^2 \rangle^{3/2} = 0.09$ , and  $\langle (Y_I/H)^4 \rangle / \langle (Y_I/H)^2 \rangle^2 = 2.95$ , respectively. As can be seen by the shape of the PDF and by these values, the PDF of  $Y_I/H$  is near Gaussian. The upper shear layer displays similar shapes and values (the mean is, of course, positive  $\langle Y_I/H \rangle = +1.16$ ). Bisset *et al.*<sup>28</sup> and Westerweel *et al.*<sup>26</sup> also observed near Gaussian PDFs of the vertical distance of the T/NT interface.

## B. Conditional mean vorticity in relation to the distance from the interface position

Figure 8 shows conditional mean profiles of  $\langle \Omega \rangle_I$ ,  $\langle |\Omega_x| \rangle_I$ ,  $\langle |\Omega_y| \rangle_I$ ,  $\langle |\Omega_z| \rangle_I$ , and  $\langle \Omega_z \rangle_I$  (nondimensionalized by  $U_1/H$ ) in relation to the distance from the T/NT interface  $Y_I$ , which is nondimensionalized by the value of the Kolmogorov microscale at the jet shear layer. The vorticity modulus shows a sharp transition from the irrotational to the turbulent zone, where it reaches a plateau with  $\langle \Omega \rangle_I \approx 4.5(U_1/H)$ , and both  $\langle \Omega_z \rangle_I$  and  $\langle |\Omega_z| \rangle_I$  show a peak very close to the interface. The shape and magnitudes of these profiles are in very good agreement with the results of Bisset *et al.*<sup>27,28</sup> and Westerweel *et al.*<sup>26,29</sup>

In the remainder of this work, the conditional mean profile of  $\langle |\Omega_z| \rangle_I$  will be used as a reference to indicate several locations near the T/NT interface. Notice that in a plane jet, this is the only nonzero mean vorticity component, i.e.,  $\langle \Omega_z(x, y, z) \rangle = \langle \Omega_z(y) \rangle \neq 0$ , while  $\langle \Omega_x(x, y, z) \rangle = \langle \Omega_y(x, y, z) \rangle = 0$ .

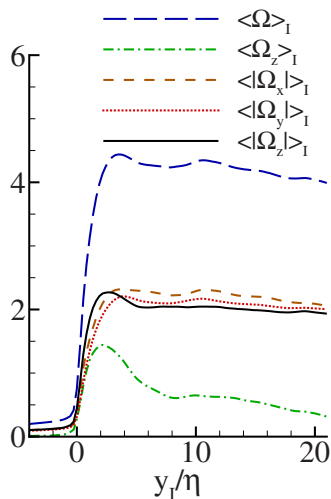


FIG. 8. (Color online) Mean conditional profiles of  $\langle \Omega \rangle_I$ ,  $\langle \Omega_z \rangle_I$ ,  $\langle |\Omega_x| \rangle_I$ ,  $\langle |\Omega_y| \rangle_I$ , and  $\langle |\Omega_z| \rangle_I$  (all normalized by  $U_1/H$ ).

=0. Moreover, as shown in Fig. 8, the gradient of this vorticity component is slightly steeper than either  $\langle |\Omega_x| \rangle_I$  or  $\langle |\Omega_y| \rangle_I$ , which is in agreement with the predictions by Reynolds<sup>32</sup> (experimentally confirmed by Werterweel *et al.*<sup>26</sup>) since this component is connected with the existence of a finite jump in the tangential velocity at the T/NT interface. However, it must be stressed that any other vorticity component might be used instead, particularly since, as remarked by a referee, there is almost no difference between the conditional mean profiles of the three vorticity components shown in Fig. 8. Finally, in the present work, three particular locations in relation to the distance from the T/NT interface will be frequently considered:  $y_1/\eta=0.0$ , which is exactly at the T/NT interface,  $y_1/\eta=1.7$ , which is close to the point of maximum  $\langle |\Omega_z| \rangle_I$ , and  $y_1/\eta=8.6$ , which is already well inside the turbulent zone.

#### IV. INVARIANTS OF THE VELOCITY GRADIENT, RATE-OF-STRAIN, AND RATE-OF-ROTATION TENSORS ACROSS THE T/NT INTERFACE

In this section, the invariants of the velocity gradient, rate-of-strain, and rate-of-rotation tensors are used to study the dynamics, topology, and geometry of the flow during the turbulent entrainment process. We start by recalling the definitions of the invariants, their relationships, and physical meanings (Sec. IV A). The next sections successively analyze the geometry of the dissipation through the invariants  $Q_W$  and  $Q_S$  (Sec. IV B), the geometry of the straining of the fluid elements through the invariants  $Q_S$  and  $R_S$  (Sec. IV C), and, finally, the relation between the flow topology and the production/dissipation of enstrophy by vortex stretching/compression through the invariants  $Q$  and  $R$  (Sec. IV D). The analysis uses conditional mean profiles of the invariants in relation to the distance from the T/NT interface, “trajectories” of these conditional mean values in their associated phase maps, and joint PDFs of the invariants at several distances from the T/NT interface.

#### A. Definitions of the invariants and associated physical meanings

The goal of this section is to review some of the background material related to the invariants of the velocity gradient, rate-of-strain, and rate-of-rotation tensors. Extensive reviews of this material can be found in Chong *et al.*,<sup>1</sup> Cantwell,<sup>3</sup> Soria and Cantwell,<sup>16</sup> Perry and Chong,<sup>4</sup> Soria *et al.*,<sup>8</sup> Blackburn *et al.*,<sup>9</sup> Ooi *et al.*,<sup>7</sup> and Wang *et al.*<sup>20</sup>

The velocity gradient tensor  $A_{ij} = \partial u_i / \partial x_j$  can be split into a symmetric and a skew-symmetric component,

$$A_{ij} = S_{ij} + \Omega_{ij}, \quad (5)$$

where  $S_{ij} = \frac{1}{2}(\partial u_i / \partial x_j + \partial u_j / \partial x_i)$  and  $\Omega_{ij} = \frac{1}{2}(\partial u_i / \partial x_j - \partial u_j / \partial x_i)$  are the rate-of-strain and rate-of-rotation tensors, respectively.

The velocity gradient tensor  $A_{ij}$  has the following characteristic equation:

$$\lambda_i^3 + P\lambda_i^2 + Q\lambda_i + R = 0, \quad (6)$$

where  $\lambda_i$  are the eigenvalues of  $A_{ij}$ . The first, second, and third invariants of the velocity gradient tensor are

$$P = -A_{ii} = -S_{ii}, \quad (7)$$

$$Q = -\frac{1}{2}A_{ij}A_{ji} = \frac{1}{4}(\Omega_i\Omega_i - 2S_{ij}S_{ij}), \quad (8)$$

and

$$R = -\frac{1}{3}A_{ij}A_{jk}A_{ki} = -\frac{1}{3}(S_{ij}S_{jk}S_{ki} + \frac{3}{4}\Omega_i\Omega_jS_{ij}), \quad (9)$$

respectively, where  $\Omega_i = \varepsilon_{ijk}\partial u_j / \partial x_k$  is the vorticity field ( $P=0$  in incompressible flow).

Similarly, the invariants of the rate-of-strain tensor are defined by its characteristic equation. The independent invariants of  $S_{ij}$  are

$$Q_S = -\frac{1}{2}S_{ij}S_{ij} \quad (10)$$

and

$$R_S = -\frac{1}{3}S_{ij}S_{jk}S_{ki}. \quad (11)$$

Finally, the only invariant of the rate-of-rotation tensor is

$$Q_W = \frac{1}{2}\Omega_{ij}\Omega_{ij} = \frac{1}{4}\Omega_i\Omega_i. \quad (12)$$

Notice that the invariants of  $S_{ij}$  are obtained by setting  $\Omega_{ij}$  to zero in Eqs. (8) and (9), while the only invariant of  $\Omega_{ij}$  is obtained by setting  $S_{ij}$  to zero in Eq. (8). It is important to recall the physical meaning of these invariants (see, e.g., Soria *et al.*,<sup>8</sup> Blackburn *et al.*,<sup>9</sup> Wang *et al.*,<sup>20</sup> and also Davidson<sup>53</sup>).

Starting with  $Q_W = \Omega_i\Omega_i/4$ , note that this invariant is related to the second invariants of  $A_{ij}$  and  $S_{ij}$  through  $Q_W = Q - Q_S$ . Therefore,  $Q_W$  is proportional to the enstrophy density ( $\Omega^2/2 = \Omega_i\Omega_i/2$ ). Regions of intense enstrophy tend to be concentrated in tubelike structures in many turbulent flows such as isotropic turbulence,<sup>54</sup> mixing layers,<sup>55</sup> and jets.<sup>41</sup>

The second invariant of  $S_{ij}$ ,  $Q_S = -S_{ij}S_{ij}/2$ , is proportional to the local rate of viscous dissipation of kinetic energy since  $\varepsilon = 2\nu S^2 = -4\nu Q_S$ , where  $S^2/2 = S_{ij}S_{ij}/2$  is the strain product. In isotropic turbulence, intense values of viscous dissipation tend to be concentrated in structures with

the form of sheets or ribbons.<sup>56</sup> On the other hand, the third invariant of  $S_{ij}$ ,  $R_S = -S_{ij}S_{jk}S_{ki}/3$ , is proportional to the strain skewness  $S_{ij}S_{jk}S_{ki}$ . This invariant has two important physical meanings. It appears as part of the production term in the strain product transport equation,<sup>53</sup>

$$\begin{aligned} \frac{D}{Dt} \left( \frac{1}{2} S_{ij} S_{ij} \right) = & -S_{ij} S_{jk} S_{ki} - \frac{1}{4} \Omega_i \Omega_j S_{ij} - S_{ij} \frac{\partial^2 p}{\partial x_i \partial x_j} \\ & + \nu S_{ij} \nabla^2 S_{ij}. \end{aligned} \quad (13)$$

As can be seen, a positive value of  $R_S$  is associated with the production of strain product (and thus of viscous dissipation), whereas  $R_S < 0$  implies a destruction of strain product. Moreover, it can be shown that  $R_S = -(\alpha_S^3 + \beta_S^3 + \gamma_S^3)/3 = -\alpha_S \beta_S \gamma_S$ , where  $\alpha_S \geq \beta_S \geq \gamma_S$  are the three eigenvalues of  $S_{ij}$  arranged in descending order. Due to incompressibility  $\alpha_S + \beta_S + \gamma_S = 0$ , therefore,  $R_S > 0$  implies that  $\alpha_S, \beta_S > 0$ ,  $\gamma_S < 0$  and the associated flow structure is sheetlike. If  $R_S < 0$ , then  $\alpha_S > 0$ ,  $\beta_S, \gamma_S < 0$ , which implies a tubelike structure.

Finally, the physical meaning of the invariants of  $A_{ij}$  depends on the sign of  $Q$ . If  $Q > 0$ , then the enstrophy ( $\Omega^2/2 = \Omega_i \Omega_i/2$ ) dominates over strain product ( $S^2/2 = S_{ij} S_{ij}/2$ ), whereas if  $Q < 0$ , the opposite occurs. In a Burgers vortex flow, for instance, the center of the vortex is characterized by  $Q > 0$ , while in the region around it,  $Q < 0$ , implying that the strain product (and hence viscous dissipation of kinetic energy) dominates. The meaning of  $R$  depends on the sign of  $Q$ . If  $Q \gg 0$ , then  $R \sim -\Omega_i \Omega_j S_{ij}/4$  and  $R < 0$  implies a predominance of vortex stretching over vortex compression, and if  $R > 0$ , vortex compression dominates. On the other hand, if  $Q \ll 0$ , then  $R \sim -S_{ij} S_{jk} S_{ki}/3 = -\alpha_S \beta_S \gamma_S$  and, therefore,  $R > 0$  is associated with a sheetlike structure, whereas  $R < 0$  is associated with a tubelike structure.

The invariants defined above are usually analyzed in joint PDFs combining two invariants. The most common combinations consist on the maps of  $(R, Q)$ ,  $(R_S, Q_S)$ , and  $(Q_W, -Q_S)$ . Figures 9(a)–9(c) show sketches of each one of these maps with the physical meaning associated with each particular location.

The  $(R, Q)$  map [Fig. 9(a)] allows us to infer about the relation between the local flow topology (enstrophy or strain dominated) and the enstrophy production term (vortex stretching or vortex compression) and associated geometry of the deformation of the fluid elements (contraction or expansion). The line defined by the discriminant  $D_A = 27/4 R_A^2 + Q_A^3$  divides the map into two regions. If  $D_A > 0$ , Eq. (6) has one real and two complex-conjugate roots, while if  $D_A < 0$ , the equation has two real distinct roots. In many turbulent flows, the  $(R, Q)$  map displays a strong (anti)correlation between  $R$  and  $Q$  in the region  $R > 0, Q < 0$  associated with sheetlike structures and also (although not as strong) in the region  $R < 0, Q > 0$  associated with a predominance of vortex stretching. This gives the  $(R, Q)$  map its characteristic teardrop shape that has been observed in a great variety of different turbulent flows such as isotropic turbulence,<sup>7</sup> mixing layers,<sup>8</sup> and channel flows.<sup>9</sup>

The  $(R_S, Q_S)$  map is particularly useful to analyze the geometry of the local straining (or deformation) of the fluid

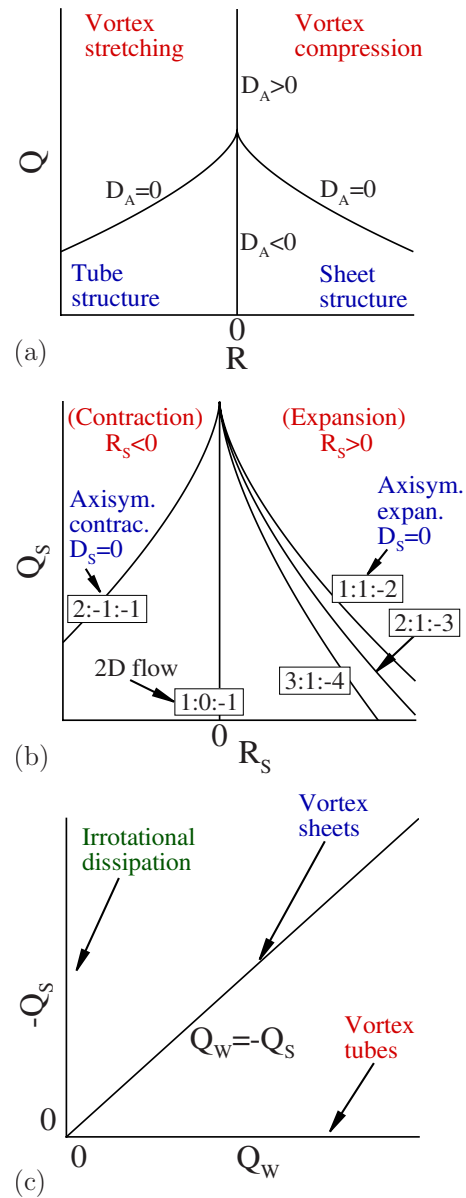


FIG. 9. (Color online) Sketch of the invariant maps of  $(R, Q)$ ,  $(R_S, Q_S)$ , and  $(Q_W, -Q_S)$  with the physical/topological features associated with each zone: (a)  $(R, Q)$  map, (b)  $(R_S, Q_S)$  map, and (c)  $(Q_W, -Q_S)$  map.

elements since  $R_S = -\alpha_S \beta_S \gamma_S$  and  $\alpha_S + \beta_S + \gamma_S = 0$  due to incompressibility. Defining the ratio of the second to the first eigenvalue of the rate-of-strain tensor  $a = \beta_S / \alpha_S$ , each value of  $a$  represents a line in the  $(R_S, Q_S)$  map defined by

$$R_S = (-Q_S)^{3/2} a(1+a)(1+a+a^2)^{-3/2}, \quad (14)$$

where each line is associated with a given flow geometry:  $\alpha_S : \beta_S : \gamma_S = 2 : -1 : -1$  (axisymmetric contraction),  $1 : 0 : -1$  (two-dimensional flow),  $3 : 1 : -4$  (biaxial stretching), and  $1 : 1 : -2$  (axisymmetric stretching). The discriminant for the  $(R_S, Q_S)$  map is defined by the line  $D_S = 27/4 R_S^2 + Q_S^3$ . Figure 9(b) shows a sketch of the  $(R_S, Q_S)$  map with several lines of constant  $a$  and their associated local flow geometry. Moreover, since  $Q_S = -\varepsilon/4\nu$ , large negative values of  $Q_S$  are associated with regions of intense kinetic energy dissipation. In many turbulent flows, the  $(R_S, Q_S)$  map shows a strong pref-

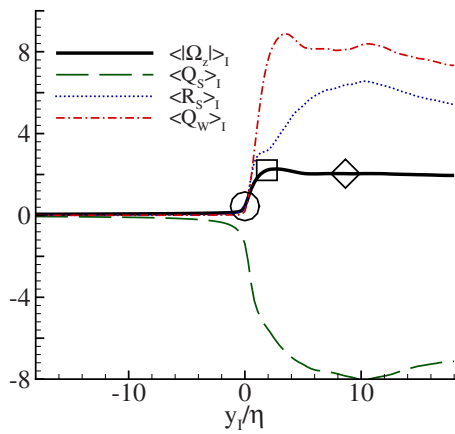


FIG. 10. (Color online) Conditional mean profiles in relation to the distance from the T/NT interface for the invariants of the rate-of-strain tensor  $\langle Q_S \rangle_I$  and  $\langle R_S \rangle_I$  and rate-of-rotation tensor  $\langle Q_W \rangle_I$ . The conditional mean profile  $\langle |\Omega_z| \rangle_I$  is also shown and the symbols mark three particular locations: (○)  $y_I/\eta=0$  (T/NT interface), (□)  $y_I/\eta=1.7$  (point of maximum  $\langle |\Omega_z| \rangle_I$ ), and (◇)  $y_I/\eta=8.6$  (well inside the turbulent region).

erence for the zone  $R_S > 0, Q_S < 0$ , indicating a predominance of sheet structures. The most probable geometry observed in several turbulent flows corresponds to a geometry of 3:1:−4 or 2:1:−3.<sup>7-9,12</sup>

Finally, the  $(Q_W, -Q_S)$  map [Fig. 9(c)] is useful to analyze the topology associated with the dissipation of kinetic energy. The horizontal line  $Q_W = \Omega_{ij}\Omega_{ij}/2$  represents points with high enstrophy but very small dissipation as in the solid body rotation at the center of a vortex tube (“vortex tubes”). On the other hand, the vertical line  $-Q_S = S_{ij}S_{ij}/2$  represents points with high dissipation but little enstrophy density. Thus, it represents points of strong dissipation outside and away from the vortex tubes (“irrotational dissipation”). The line making 45° with the vertical and horizontal lines,  $Q_W = -Q_S$ , represents points of both high dissipation and high enstrophy density, as occurs in vortex sheet structures. In compressible mixing layers, it has been shown that the smallest scale motions associated with the highest local values of dissipation (but with relatively small amounts of the total dissipation) tend to be aligned with the  $Q_W = -Q_S$  line.<sup>8</sup> However, generally, the regions of high dissipation are not correlated with regions of concentrated enstrophy.<sup>7-9</sup>

## B. Analysis of the invariants $Q_W$ and $Q_S$ across the T/NT interface

In this section, we investigate the second invariants of the rate-of-strain and rate-of-rotation tensors  $Q_W$  and  $Q_S$  near the T/NT interface in order to analyze the geometry of the dissipation. Conditional mean profiles of the invariants in relation to the distance from the T/NT interface are shown in Fig. 10 (the invariant  $\langle R_S \rangle_I$  is also shown). The conditional mean profile of the vorticity component  $\langle |\Omega_z| \rangle_I$  is also shown and the symbols mark three particular locations:  $y_I/\eta=0.0$  (T/NT interface),  $y_I/\eta=1.7$  (point of maximum of  $\langle |\Omega_z| \rangle_I$ ), and  $y_I/\eta=8.6$  (deep inside the turbulent region).

As can be seen, all the invariants display quick changes near the interface, as does  $\langle |\Omega_z| \rangle_I$ . We start with the invariant

of the rate-of-rotation tensor  $Q_W = \Omega_{ij}\Omega_{ij}/2$ . As expected, the mean profile of this invariant  $\langle Q_W \rangle_I$  is similar to the evolution of the conditional mean profile of  $\langle \Omega \rangle_I$  shown before in Fig. 8, i.e., this invariant, like the vorticity modulus, is negligible in the irrotational flow region  $y_I/\eta < 0$  and steeply rises once the T/NT interface has been crossed at  $y_I/\eta=0$ . In the turbulent region  $y_I/\eta > 0$ ,  $\langle Q_W \rangle_I$  like  $\langle \Omega \rangle_I$  is high and more or less constant, in agreement with Corrsin and Kistler,<sup>21</sup> and with the recent numerical simulations of Bisset *et al.*<sup>28</sup> and the experimental results of Westerweel *et al.*<sup>26,29</sup>

The first interesting observation comes from the conditional mean profile of  $\langle Q_S \rangle_I$ . This invariant is negligible in the irrotational flow region and far away from the T/NT interface,  $y_I/\eta < -8$ . However,  $\langle Q_S \rangle_I$  begins to increase (in modulus) in the irrotational region from  $y_I/\eta > -8$  onward until very close to the T/NT interface, at  $y_I/\eta \approx -1.7$ , the invariant  $\langle Q_S \rangle_I$  displays values of the order of  $\langle Q_S \rangle_I \approx -0.2(U_1/H)^2$ . Since  $\langle Q_S \rangle_I = -\langle S_{ij}S_{ij} \rangle_I/2$  is proportional to the dissipation rate, this means that non-negligible viscous dissipation of kinetic energy occurs in the irrotational flow region near the T/NT interface. At first sight, this result seems surprising. How can it be that viscous dissipation of kinetic energy takes place in regions with almost no vorticity? More work on this subject has to be done in order to understand this mechanism. What can be said, however, is that this result is consistent with the existence of irrotational velocity fluctuations and Reynolds stresses outside the turbulent region near the T/NT interface, as observed by Westerweel *et al.*<sup>26</sup> The origin of this viscous dissipation in the irrotational region is analyzed in Appendix B following a remark made by a referee. Non-negligible values of the strain product (and thus of kinetic energy dissipation) have been recently observed by Holzner *et al.*<sup>31</sup> outside the turbulent region and close to the T/NT interface in experimental results from a turbulent front generated by an oscillating grid.

Returning to Fig. 10, we notice that once the T/NT interface is crossed,  $\langle Q_S \rangle_I$  increases (in modulus) at a faster rate than it did before in  $-8 < y_I/\eta < 0$  and reaches a more or less constant turbulent value of  $\langle Q_S \rangle_I \approx -7(U_1/H)^2$  from  $y_I/\eta > 5$  onward. It is interesting to see that the viscous dissipation of kinetic energy, i.e.,  $-4\nu\langle Q_S \rangle_I$ , needs more time than the enstrophy density, which is proportional to  $\langle Q_W \rangle_I$ , to reach its turbulent value. Indeed, we see that after  $y_I/\eta=0$ , the transition into the fully developed turbulent state is faster for  $\langle Q_W \rangle_I$  than for  $\langle Q_S \rangle_I$ :  $\langle Q_S \rangle_I$  needs the space between  $0 < y_I/\eta < 5$  to reach its turbulent value, while  $\langle Q_W \rangle_I$  reaches its peak at about  $y_I/\eta \approx 2.5$ . This suggests that the mechanism of viscous dissipation needs more time to start working to its fullest than other physical mechanisms driving the growth of vorticity during the turbulent entrainment process.

Figures 11(a) and 11(b) show the “trajectory” of the mean values of  $\langle Q_W \rangle_I$  and  $\langle -Q_S \rangle_I$  in their associated phase map. The mean values of the invariants taken from the irrotational region are represented by solid triangles, while solid inverted triangles represent points from the turbulent region. The trajectories connecting the mean values are represented by a solid line (irrotational region) and a dashed line (turbulent region). Again, the symbols mark three particular loca-

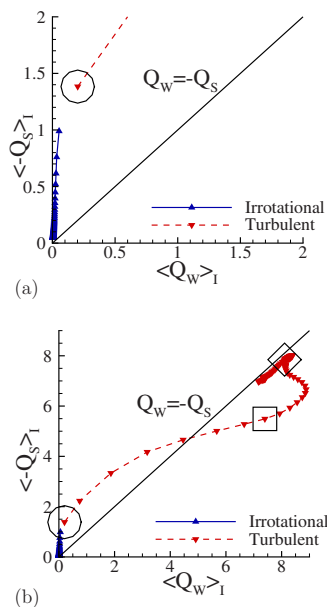


FIG. 11. (Color online) Trajectories of the conditional mean values of the second invariants of the rate-of-rotation tensor  $\langle Q_W \rangle_I$  and rate-of-strain tensor  $\langle Q_S \rangle_I$  in their associated phase map for (a)  $0 < \langle Q_W \rangle_I < 2$  and  $0 < \langle -Q_S \rangle_I < 2$  and (b)  $0 < \langle Q_W \rangle_I < 9$  and  $0 < \langle -Q_S \rangle_I < 9$ . The solid line and solid triangles indicate points in the irrotational region  $y_l/\eta \leq 0$ , while the dashed line and solid inverted triangles indicate points in the turbulent region  $y_l/\eta > 0$ . The symbols mark (○)  $y_l/\eta = 0$ , (□)  $y_l/\eta = 1.7$ , and (◇)  $y_l/\eta = 8.6$ .

tions:  $y_l/\eta = 0.0$  (T/NT interface),  $y_l/\eta = 1.7$  ( $\langle |\Omega_z| \rangle_I$  maximum), and  $y_l/\eta = 8.6$  (deep inside the turbulent region). In the irrotational region, the mean values of the invariants are near the vertical line defined by  $\langle Q_W \rangle_I = 0$ . This line marks flow points with high dissipation but little enstrophy; thus, the mean geometry of the dissipation at the T/NT interface is characterized by irrotational dissipation. The interface region is crossed at  $\langle Q_W \rangle_I \approx 0.2$  and  $\langle -Q_S \rangle_I \approx 1.4$ . After this, the flow topology detaches from the vertical line  $\langle Q_W \rangle_I = 0$  and approaches the line  $\langle Q_W \rangle_I = \langle -Q_S \rangle_I$ , indicating a predominance of vortex sheets in the flow inside the turbulent region. It is interesting to see how the mean flow topology moves in the  $(Q_W, -Q_S)$  phase map as the flows goes from the T/NT interface into the point of maximum  $\langle |\Omega_z| \rangle_I$ . It starts to be roughly at the middle of the lines  $\langle Q_W \rangle_I = 0$  and  $\langle Q_W \rangle_I = \langle -Q_S \rangle_I$ , before turning into the region between the lines  $\langle Q_W \rangle_I = \langle -Q_S \rangle_I$  and  $\langle -Q_S \rangle_I = 0$ . This may imply a mixed tendency for irrotational dissipation and vortex sheets, followed by a mixed tendency for vortex sheets and vortex tubes. After the point of maximum  $\langle |\Omega_z| \rangle_I$  has been crossed, at  $(Q_W, -Q_S) \approx (7.5, 5.0)$ , the mean flow topology falls suddenly into the line  $\langle Q_W \rangle_I = \langle -Q_S \rangle_I$ .

Figures 12(a)–12(c) show joint PDFs of  $(Q_W, -Q_S)$  at the three particular locations used before:  $y_l/\eta = 0.0, 1.7$ , and  $8.6$ . Following common practice, the invariants were nondimensionalized with  $\langle S_{ij} S_{ij} \rangle$ . At the T/NT interface  $y_l/\eta = 0.0$ , the joint PDF of  $(Q_W, -Q_S)$  shows a marked tendency to be aligned with the vertical line defined by  $Q_W = 0$ , which attests a strong predominance of dissipation (strain product) over enstrophy, i.e., irrotational dissipation dominates at the T/NT

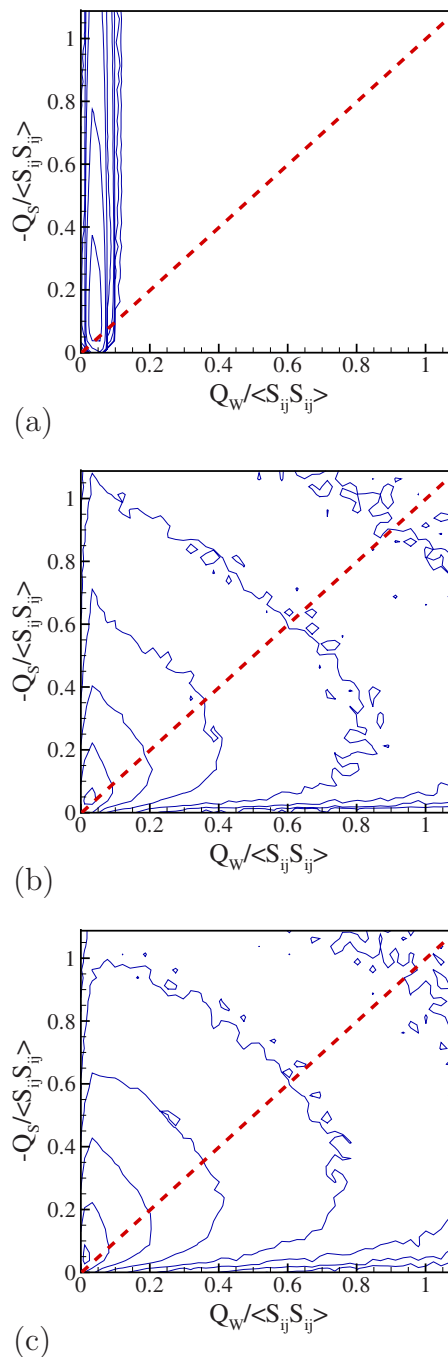


FIG. 12. (Color online) Joint PDFs of  $Q_W$  and  $-Q_S$  at (a)  $y_l/\eta = 0$ , (b)  $y_l/\eta = 1.7$ , and (c)  $y_l/\eta = 8.6$ . The contour levels are 0.01, 0.03, 0.1, 0.3, 1, 3, 10, and 30.

interface, for all the scales of motion. Notice that the probability of having points with  $Q_W/\langle S_{ij} S_{ij} \rangle > 0.14$  is virtually zero, i.e., virtually all the points from the T/NT interface are associated with irrotational dissipation, a fact that was already observed for the “mean” values of this invariant map. As described in the previous section, the large scale flow vortices are characterized by near solid body rotation with little dissipation. Thus, the shape of this joint PDF suggests the total absence of large scale vortex tubes at the T/NT interface. This result is not surprising considering that these tube structures need some time to be generated and also

some room to occupy. At the point of maximum  $\langle |\Omega_z| \rangle_I$ ,  $y_I/\eta=1.7$  as in deep inside the turbulent zone  $y_I/\eta=8.6$ , the shape of the joint PDFs is quite similar and resembles the shape of the joint PDFs obtained in isotropic turbulence by Ooi *et al.*<sup>7</sup> and in a turbulent channel flow by Blackburn *et al.*<sup>9</sup> Notice that here, for the contour lines associated with the most frequent values (and with the scales responsible for the bulk of the dissipation), there is still some tendency of the lines to be aligned with the vertical line  $Q_W=0$ ; however, the most intense values, associated with rare events at the smallest scales of motion (but with a relatively small amount of dissipation) seem to be aligned with the horizontal line  $-Q_S=0$  associated with vortex tubes. Indeed, as in Ooi *et al.*,<sup>7</sup> the contour lines of intense values of  $Q_W$  are slightly skewed toward the axis  $-Q_S=0$ , which suggests that intense values of  $Q_W$  correspond to much smaller values of  $-Q_S$ , i.e., the high  $Q_W$  regions are associated with solid body rotation with little energy dissipation. This suggests that at both  $y_I/\eta=1.7$  and  $y_I/\eta=8.6$ , the flow already has some of its characteristic large scale coherent vortices. However, since  $Q_W$  and  $-Q_S$  are related to local (not global) features of the flow, the examination of the coherent vortices in relation to the distance from the T/NT interface should be addressed carefully in a future study. Finally, notice that in contrast to the mean values of these invariants shown before in Fig. 11, there is here no discernible tendency for an alignment along the line,  $Q_W=-Q_S$ , associated with vortex sheet structures. This implies that in this case, the mean result obtained before in the  $(Q_W, -Q_S)$  phase map is just a consequence of the averaging procedure, i.e., there is no clear tendency for the flow to be dominated by vortex sheet structures. The results point instead to a topology inside the turbulent region where both vortex tubes, vortex sheets, and zones of irrotational dissipation exist.

### C. Analysis of the invariants $Q_S$ and $R_S$ across the T/NT interface

In this section, we investigate the second and third invariants of the rate-of-strain tensor  $Q_S$  and  $R_S$  near the T/NT interface in order to analyze the geometry of straining of the fluid elements. Conditional mean profiles of these invariants in relation to the distance from the T/NT interface were shown before in Fig. 10 with the conditional mean profile of the vorticity component  $\langle |\Omega_z| \rangle_I$  and the symbols marking three particular locations:  $y_I/\eta=0.0, 1.7$ , and  $8.6$ .

The evolution of the mean invariant  $\langle Q_S \rangle_I$  was already analyzed in Sec. IV B. As for the invariant  $\langle R_S \rangle_I$ , one can see that it is negligible for  $y_I/\eta < 0$ , which implies that the observed growth of viscous dissipation observed in that region is not caused by the strain product production term  $-S_{ij}S_{jk}S_{ki}$  [see Eq. (13)]. Indeed,  $\langle R_S \rangle_I$  starts to grow only after the T/NT interface has been crossed. Notice that like  $\langle Q_S \rangle_I$ , it seems that  $\langle R_S \rangle_I$  needs more time to reach its turbulent value of  $\langle R_S \rangle_I \approx 6.5(U_1/H)^3$  than the enstrophy. Finally, note that throughout the flow (including the irrotational region where  $\langle R_S \rangle_I$  is very small), we always have  $\langle R_S \rangle_I > 0$ , implying that the mean flow structure is always sheetlike.

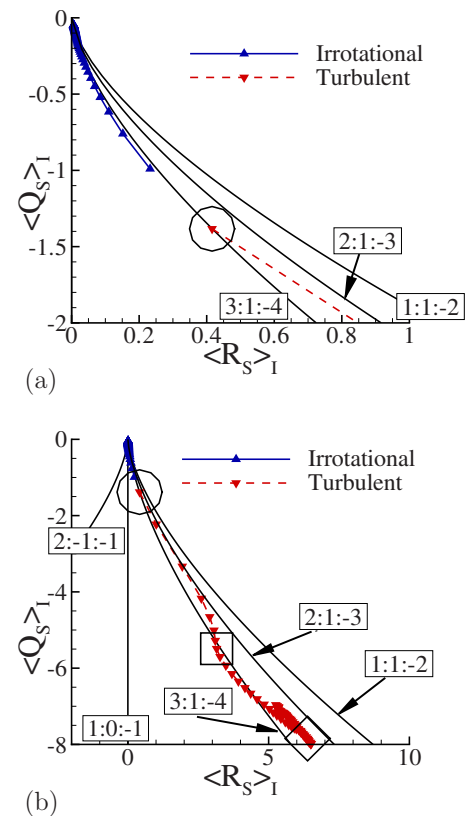


FIG. 13. (Color online) Trajectories of the conditional mean values of the invariants of the rate-of-strain tensors  $\langle R_S \rangle_I$  and  $\langle Q_S \rangle_I$  in their associated phase map for (a)  $0 < \langle R_S \rangle_I < 1$  and  $-2 < \langle Q_S \rangle_I < 0$  and (b)  $0 < \langle R_S \rangle_I < 10$  and  $-8 < \langle Q_S \rangle_I < 0$ . The solid line and solid triangles indicate points in the irrotational region  $y_I/\eta \leq 0$ , while the dashed line and solid inverted triangles represent points from the turbulent region  $y_I/\eta > 0$ . The symbols mark three particular locations: (O)  $y_I/\eta=0$  (T/NT interface), (□)  $y_I/\eta=1.7$  (point of maximum  $\langle |\Omega_z| \rangle_I$ ), and (◇)  $y_I/\eta=8.6$  (well inside the turbulent region).

Figures 13(a) and 13(b) show the trajectory of the mean values of  $\langle Q_S \rangle_I$  and  $\langle R_S \rangle_I$  in their associated phase map. Again, the mean values of the invariants taken from the irrotational region are represented by solid triangles, while solid inverted triangles represent points from the turbulent region. The trajectories connecting the mean values are represented by a solid line (irrotational region) and a dashed line (turbulent region), and the symbols mark the T/NT interface, the point of maximum  $\langle |\Omega_z| \rangle_I$ , and a location placed deep inside the turbulent region. In the entire flow region, we see that the invariants are in the region  $\langle R_S \rangle_I > 0$  and  $\langle Q_S \rangle_I < 0$ , i.e., the mean flow geometry is associated with the expansion of the fluid elements. In the irrotational region, the mean flow topology is  $3:1:-4$  and changes to  $2:1:-3$  between the T/NT interface and the point of maximum  $\langle |\Omega_z| \rangle_I$ . Shortly before the point of maximum  $\langle |\Omega_z| \rangle_I$ , the flow geometry turns again into  $3:1:-4$ , where it stays some time. Finally, the mean flow topology becomes somewhere in the middle of these two lines, i.e., near  $\frac{5}{2}:1:-\frac{7}{2}$ . Recall that the most probable eigenvalue ratios observed in several works are  $3:1:-4$  and  $2:1:-3$ .

Figures 14(a)–14(c) show joint PDFs of  $(R_S, Q_S)$  at the three particular locations used before:  $y_I/\eta=0.0, 1.7$ , and  $8.6$ . The three joint PDFs are not fundamentally different,

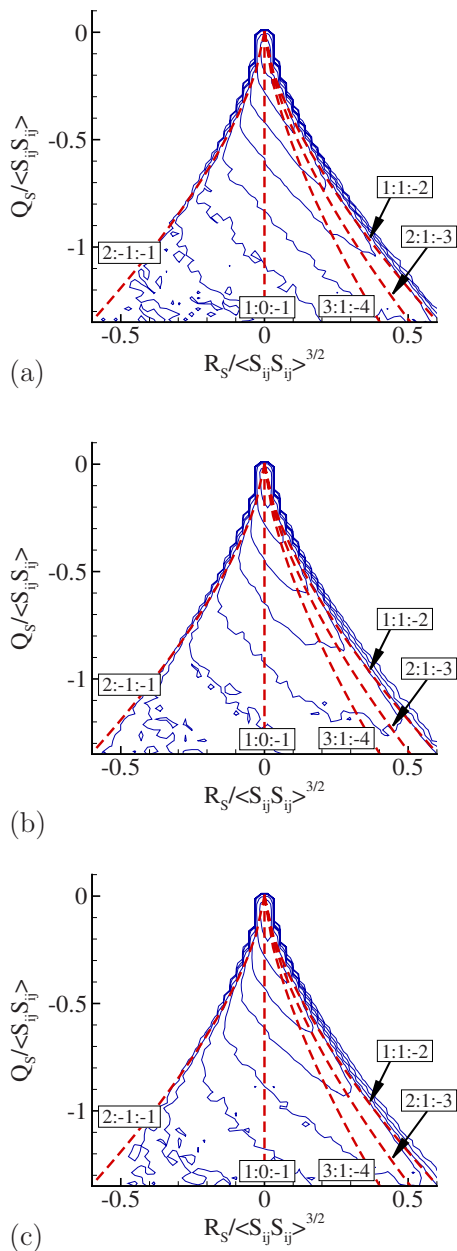


FIG. 14. (Color online) Joint PDFs of  $R_S$  and  $Q_S$  at (a)  $y_l/\eta=0$ , (b)  $y_l/\eta=1.7$ , and (c)  $y_l/\eta=8.6$ . The contour levels are the same as in Fig. 12.

i.e., all show a clear preference for the region  $R_S > 0$  and  $Q_S < 0$  associated with extensive straining of the fluid elements, although contractive straining also exists at some (much fewer) points. The alignments of the contour lines of the joint PDF at the T/NT interface shows that the most frequent values seem to show a tendency toward 2:1:-3 [see Fig. 14(a)], while intermediate values seem to be closer to 1:1:-2, i.e., the smaller scales of motion at the T/NT interface are associated with near axisymmetric extension. At the point of maximum  $\langle |\Omega_z| \rangle_I$  at  $y_l/\eta=1.7$  and deep inside the turbulent region at  $y_l/\eta=8.6$ , the joint PDFs are quite similar [compare Figs. 14(b) and 14(c)]. Here, the contour lines are aligned with 2:1:-3 for the most frequent, intermediate, and less frequent values.

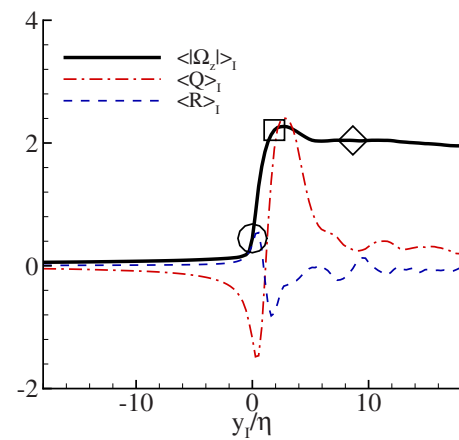


FIG. 15. (Color online) Conditional mean profiles in relation to the distance from the T/NT interface for the invariants of the velocity gradient tensor  $\langle Q \rangle_I$  and  $\langle R \rangle_I$ . The conditional mean profile  $\langle |\Omega_z| \rangle_I$  is also shown and the symbols mark (○)  $y_l/\eta=0$ , (□)  $y_l/\eta=1.7$ , and (◇)  $y_l/\eta=8.6$ .

#### D. Analysis of the invariants $Q$ and $R$ across the T/NT interface

This section analyzes the second and third invariants of the velocity gradient tensor  $Q$  and  $R$  near the T/NT interface in order to analyze the relation between the flow topology and dynamics. Conditional mean profiles of the invariants in relation to the distance from the T/NT interface are shown in Fig. 15. The conditional mean profile of the vorticity component  $\langle |\Omega_z| \rangle_I$  is also shown and the symbols mark  $y_l/\eta=0.0$ , 1.7, and 8.6.

The invariant  $Q = (\Omega_i \Omega_i - 2S_{ij} S_{ij})/4$  shows that in the irrotational flow region,  $\langle Q \rangle_I \approx \langle Q_S \rangle_I < 0$ , as expected since in this region there is virtually no vorticity and, therefore, the evolution of  $\langle Q \rangle_I$  is dominated by the increase of strain product (and viscous dissipation) described before.  $\langle Q \rangle_I$  reaches a minimum of  $\langle Q \rangle_I \approx -1.3(U_1/H)^2$  at  $y_l/\eta=0.5$  shortly after the T/NT interface  $\langle Q \rangle_I$  begins to grow and becomes positive at  $y_l/\eta \approx 1.2$ , implying that from that point onward the enstrophy density dominates over strain product. Recall that the strain product (and thus viscous dissipation) increases at a smaller rate than the vorticity (and enstrophy density) in the region  $0 < y_l/\eta < 5$ . This invariant attains a maximum at about  $y_l/\eta \approx 2.5$  (shortly after the maximum of  $\langle |\Omega_z| \rangle_I$ ), before falling to  $\langle Q \rangle_I \approx 0$  for  $y_l/\eta > 8$ . Notice that  $\langle Q \rangle_I = 0$  in isotropic turbulence and, as shown by da Silva and Pereira,<sup>36</sup> and also as confirmed in the present work, the plane jet is, in many ways, close to isotropic at the center of the shear layer. The evolution of  $\langle Q \rangle_I$  just described underlines the interplay between enstrophy and strain during the first stages of the turbulent entrainment. Strain dominates over enstrophy in the irrotational region near the T/NT interface (enstrophy is virtually zero there), while enstrophy dominates over strain at the start of the turbulent region, where, as discussed above, strain product (and also strain skewness) do not increase as fast as the enstrophy. Deep inside the turbulent region, the enstrophy and strain product are comparable, as in isotropic turbulence.

The conditional mean of the third invariant of the velocity gradient tensor  $R = -[S_{ij} S_{jk} S_{ki} + (3/4)\Omega_i \Omega_j S_{ij}]_I$  is zero or

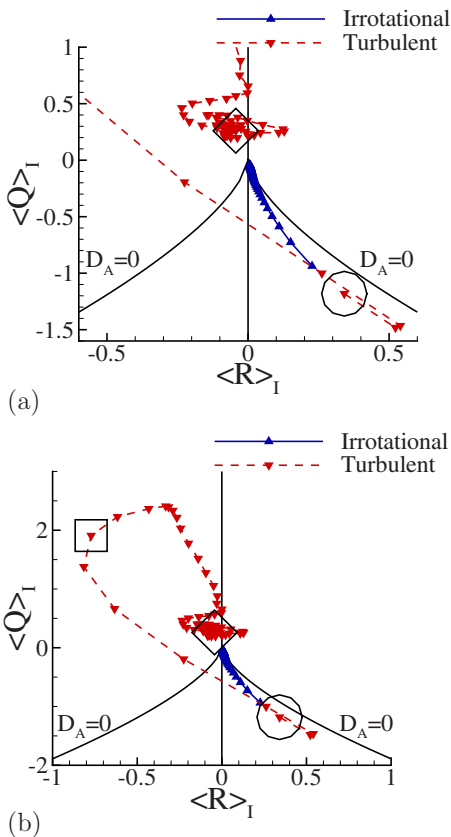


FIG. 16. (Color online) Trajectories of the conditional mean values of the invariants of the velocity gradient tensors  $\langle R \rangle_I$  and  $\langle Q \rangle_I$  in their associated phase map for (a)  $-0.6 < \langle R \rangle_I < 0.6$  and  $-1.5 < \langle Q \rangle_I < 1$  and (b)  $-1 < \langle R \rangle_I < 1$  and  $-2 < \langle Q \rangle_I < 3$ . The solid line and solid triangles indicate points in the irrotational region  $y_I/\eta \leq 0$ , while the dashed line and solid inverted triangles indicate points in the turbulent region  $y_I/\eta > 0$ . The symbols mark (○)  $y_I/\eta = 0$  (T/NT interface), (□)  $y_I/\eta = 1.7$  (point of maximum  $\langle |\Omega_z| \rangle_I$ ), and (◇)  $y_I/\eta = 8.6$  (well inside the turbulent region).

negligible in the whole irrotational region,  $\langle R \rangle_I \approx 0$ , in  $y_I/\eta < 0$ . Once the T/NT interface has been crossed,  $R$  grows and reaches a positive maximum of  $\langle R \rangle_I \approx 0.5(U_1/H)^3$  at  $y_I/\eta \approx 0.5$ . Since in this region  $\langle Q \rangle_I$  is high and negative, this implies that  $\langle R \rangle_I \sim -\langle S_{ij}S_{jk}S_{ki} \rangle_I/3 = -\langle \alpha_S \beta_S \gamma_S \rangle_I$ . Therefore, the associated flow structure is sheetlike, consistent with the discussion about  $\langle R_S \rangle_I$  described above.  $\langle R \rangle_I$  decreases after this, reaching a minimum of  $\langle R \rangle_I \approx -1.0(U_1/H)^3$  at  $y_I/\eta \approx 1.6$ . At this point,  $\langle Q \rangle_I$  is large and positive and thus  $\langle R \rangle_I \sim -\langle \Omega_i \Omega_j S_{ij} \rangle_I/4 > 0$ , i.e., (positive) enstrophy production (vortex stretching) dominates the flow. Finally, for  $y_I/\eta > 8$ ,  $\langle R \rangle_I \approx 0$ , as expected since the flow is close to isotropic and  $\langle R \rangle_I = 0$  in isotropic turbulence.

Figure 16 shows the trajectory of the mean values of  $\langle Q \rangle_I$  and  $\langle R \rangle_I$  in their associated phase map. The mean values of the invariants taken from the irrotational region are represented by solid triangles, while solid inverted triangles represent points from the turbulent region, and the trajectories connecting the mean values are represented by a solid line (irrotational region) and a dashed line (turbulent region). Again, the symbols mark  $y_I/\eta = 0, 1.7$ , and  $8.6$ . In the irrotational flow region, far away from the T/NT interface, the mean invariants are at the origin, i.e.,  $\langle R \rangle_I \approx 0$  and  $\langle Q \rangle_I \approx 0$ .

As the flow approaches the T/NT interface, the mean invariants move away from the origin and become more and more distant from the origin along the line,  $D_A = 0$ , for  $\langle R \rangle_I > 0$  and  $\langle Q \rangle_I < 0$ , which is associated with straining of fluid elements. Notice that the T/NT interface is very close to the point of maximum  $\langle R \rangle_I$  and to the point of minimum  $\langle Q \rangle_I$ . After the T/NT interface, the mean flow topology moves very quickly into the region,  $\langle R \rangle_I < 0$  and  $\langle Q \rangle_I > 0$ , associated with a predominance of vortex stretching. It is interesting to notice that the point of maximum  $\langle |\Omega_z| \rangle_I$  is located near the point that is most distant from the origin in this quadrant, indicating that the point of maximum  $\langle |\Omega_z| \rangle_I$  is connected with the maximum (mean) values of vortex stretching that occur during the turbulent entrainment process. Finally, the mean invariants fall into the region near the origin of the  $(R, Q)$  phase map, as expected since the mean values of both  $\langle R \rangle_I$  and  $\langle Q \rangle_I$  in the center of the jet shear layer are near zero, as in isotropic turbulence.

Figures 17(a)–17(c) show joint PDFs of  $(R, Q)$  at the three particular locations used before:  $y_I/\eta = 0.0$  (T/NT interface),  $y_I/\eta = 1.7$  (point of maximum  $\langle |\Omega_z| \rangle_I$ ), and  $y_I/\eta = 8.6$  (deep inside the turbulent zone). The first important observation concerns the general shape of the PDFs. At the T/NT interface, the teardrop characteristic shape of the  $(R, Q)$  phase map cannot be seen yet [see Fig. 17(a)]. The values of  $R$  and  $Q$  exist only below the lines defined by the discriminant  $D_A = 0$ . This is consistent with the results described before, i.e., at the T/NT interface, strain product dominates over enstrophy and thus  $Q < 0$  for virtually all the points of the T/NT interface, and not only in the mean, as we saw before. Notice, however, that even at the T/NT interface, the contour lines of the joint PDFs for  $R > 0$  are already aligned with the line,  $D_A = 0$ . At the points of maximum  $\langle |\Omega_z| \rangle_I$  and deep inside the turbulent region, the joint PDFs of the  $(R, Q)$  map already show the well known teardrop shape [see Figs. 17(b) and 17(c)], where  $Q$  and  $R$  are correlated in two particular regions:  $R > 0$  and  $Q < 0$  representing a predominance of biaxial stretching of the fluid elements and  $R < 0$  and  $Q > 0$  associated with a predominance of enstrophy production by vortex stretching. It is impressive to observe how quickly and how so close to the T/NT interface this teardrop shape appears: the flow needs a length of less than  $1.7\eta$  to form the classical teardrop shape. Also, note that the shape of the joint PDFs in  $y_I/\eta = 1.7$  and  $y_I/\eta = 8.6$  shown in Figs. 17(b) and 17(c) is very similar and is similar also to the joint PDFs of these quantities in numerous works.<sup>3,7-9,19,20</sup> The only (small) difference between Figs. 17(b) and 17(c) is that the alignment of the contours with the line  $D_A = 0$  for  $R > 0$  is stronger at  $y_I/\eta = 8.6$  than in  $y_I/\eta = 1.7$  and also that the intermediate contour lines are a bit more squeezed in the horizontal direction near the origin for  $y_I/\eta = 1.7$  than for  $y_I/\eta = 8.6$ . This fact again suggests that there are still some adjustments going on within the flow between  $y_I/\eta = 1.7$  and  $y_I/\eta = 8.6$ , although the overall shape of the joint PDFs are similar in both locations.

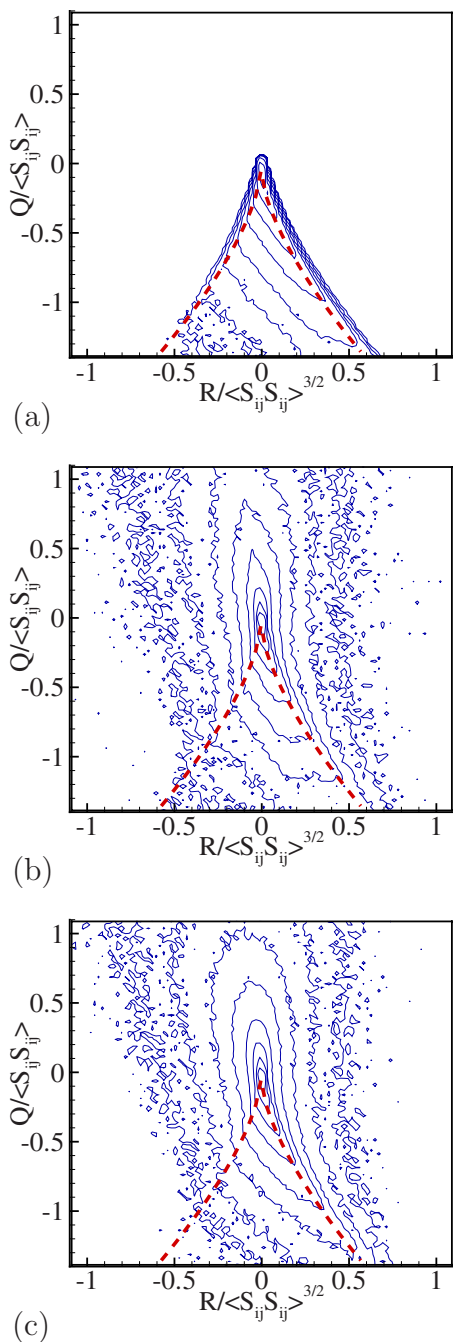


FIG. 17. (Color online) Joint PDFs of  $R$  and  $Q$  at three particular locations: (a)  $y_l/\eta=0$  (T/NT interface), (b)  $y_l/\eta=1.7$  (point of maximum  $\langle |\Omega_z| \rangle_I$ ), and (c)  $y_l/\eta=8.6$  (well inside the turbulent region). The contour levels are the same as in Fig. 12.

## V. CONCLUSIONS

The invariants of the velocity gradient ( $R$  and  $Q$ ), rate-of-strain ( $R_S$  and  $Q_S$ ), and rate-of-rotation ( $Q_W$ ) tensors were analyzed near the T/NT interface, which is present in many flows such as mixing layers, wakes, and jets, using a DNS of a turbulent plane jet at  $Re_\lambda \approx 120$ . The invariants were analyzed by using conditional mean values in relation to the distance from the T/NT interface, their associated trajectories in the classical phase maps, and joint PDFs at several distances from the T/NT interface.

The mean and instantaneous value of all the invariants is

zero in the irrotational flow region far away from the T/NT interface. As the T/NT interface is approached from the irrotational flow region, the mean and instantaneous value of most of the invariants remains zero. However, we see that  $\langle Q \rangle_I = \langle Q_S \rangle_I < 0$  and these invariants are seen to increase (in modulus) rapidly. This implies the existence of viscous dissipation of kinetic energy outside the turbulent region. A similar result was recently obtained by Holzner *et al.*<sup>31</sup> near the turbulent front generated by an oscillating grid. Moreover, we observed also that not only the mean value of  $Q$  is negative  $\langle Q \rangle_I < 0$  but also that the same is true for all points located at  $-5 < y_l/\eta < 0$ , i.e.,  $Q < 0$  everywhere, thereby implying that strain product dominates over enstrophy in all flow points from this region. The physical mechanism responsible for this irrotational dissipation still has to be explained; however, the analysis of the invariant  $R_S$  shows that the strain product production term—see Eq. (13)—is negligible outside the turbulent region and thus cannot explain the high level of viscous dissipation found there. Either viscous effects or nonlocal effects related to the pressure field are responsible for this irrotational viscous dissipation. Preliminary results discussed in Appendix B seem to imply that this irrotational dissipation is caused by instantaneous (local) pure shear induced by the large scale entraining motions. Finally, although  $\langle R_S \rangle_I \approx 0$ , its value is always positive, which implies that the mean flow geometry is already characterized by the straining (as opposed to the contraction) of the fluid elements. In particular, the mean values of  $\langle R_S \rangle_I$  and  $\langle Q_S \rangle_I$  show a preference for a geometry characterized by  $\alpha_S : \beta_S : \gamma_S = 3 : 1 : -4$  in this region, where  $\alpha_S$ ,  $\beta_S$ , and  $\gamma_S$  are the eigenvalues of the rate-of-strain tensor arranged in descending order.

Right at the T/NT interface, the enstrophy density is still negligible as attested by the local and mean values of the invariant of the rate-of-rotation tensor  $Q_W \approx 0$ , but on the other hand, the local and mean values of the strain product, proportional to  $-\langle Q_S \rangle_I$ , are very high. The joint PDF of  $Q_W$  and  $-Q_S$  shows that at the T/NT interface, all the flow points are characterized by irrotational dissipation, i.e., there is still no sign of the coherent vortices that are known to exist in the turbulent region. Moreover, the analysis of the invariants  $R$  and  $Q$  show that the classical teardrop shape of the  $(R, Q)$  phase map is not yet formed at the T/NT interface.

All the invariants display rapid changes shortly after the T/NT interface. In particular, the invariants show that the geometry and topology of the flow rapidly evolves from the T/NT interface until the point of maximum  $\langle |\Omega_z| \rangle_I$  located at  $y_l/\eta=1.7$ . The invariant  $\langle Q_W \rangle_I$  rapidly grows and reaches values which stay more or less constant afterward throughout the whole turbulent region. The invariants  $\langle Q_S \rangle_I$  and  $\langle R_S \rangle_I$ , proportional to the viscous dissipation rate and strain skewness, respectively, also increase during this time, although at a smaller rate. Indeed, these invariants only reach their turbulent values long after the point of maximum  $\langle |\Omega_z| \rangle_I$ . Notice, however, that the geometry associated with the viscous dissipation changes quite dramatically from the T/NT interface to the point of maximum  $\langle |\Omega_z| \rangle_I$ , as can be appreciated in the joint PDF of  $Q_W$  and  $-Q_S$ . The contour lines of these

curves at  $y_I/\eta=1.7$  are already very similar to the ones observed in isotropic turbulence by Ooi *et al.*<sup>7</sup> and also in a turbulent channel flow by Blackburn *et al.*<sup>9</sup> There is still some tendency for the contour lines associated with the most frequent values to be aligned with the vertical line  $-Q_S=S_{ij}S_{ij}/2$  associated with irrotational dissipation, but in most of the contour lines, no correlation can be observed between  $Q_W$  and  $-Q_S$ . The smaller values of the contour lines seem to be tilted to the horizontal line  $-Q_S=0$ , which implies that the highest values of  $Q_W$ , representing points with very high values of enstrophy, are associated with little viscous dissipation, as in the case of a solid body rotation. This suggests that at this point  $y_I/\eta=1.7$ , large scale coherent vortices already exist in the flow. Furthermore, the contour lines of the joint PDF between  $R_S$  and  $Q_S$  show that during the initial entrainment phase i.e., for  $0 < y_I/\eta < 1.7$ , the local flow topology is characterized by  $\alpha_S:\beta_S:\gamma_S=2:1:-3$ . The most interesting result observed at  $y_I/\eta=1.7$  is related to the analysis of the  $R$  and  $Q$  invariants and their phase map. The joint PDF of these invariants already shows the classical teardrop shape observed in experimental and numerical studies of many turbulent flows. It is remarkable that the flow needs less than  $1.7\eta$ , since crossing of the T/NT interface, to form the teardrop shape completely. Moreover, the mean values of these invariants show that the point of maximum  $\langle|\Omega_z|\rangle_I$  is very close to the point of maximum  $\langle Q\rangle_I$  and the point of minimum  $\langle R\rangle_I$ . This implies that the maximum of  $\langle|\Omega_z|\rangle_I$  is near the point of maximum (mean) vortex stretching.

Finally, from  $y_I/\eta=1.7$  to  $y_I/\eta=8.6$ , few things seem to change during the turbulent entrainment process. Indeed, several invariants and joint PDFs at  $y_I/\eta=1.7$  and  $y_I/\eta=8.6$  are very similar, e.g., the joint PDFs of  $(Q_W, -Q_S)$ ,  $(R_S, Q_S)$ , and  $(R, Q)$ . However, a closer look into the invariants shows that this is not really the case. For instance, the mean invariants  $\langle Q_S\rangle_I$  and  $\langle R_S\rangle_I$  still increase to their turbulent values after the point of maximum  $\langle|\Omega_z|\rangle_I$  has been crossed at  $y_I/\eta=1.7$ . This suggests that between  $y_I/\eta=1.7$  and  $y_I/\eta=8.6$ , there are still some physical adjustment processes going on within the flow. The nature of these processes should be analyzed in future works.

## ACKNOWLEDGMENTS

The authors would like to acknowledge an anonymous referee for many interesting and important remarks made during the revision of this work. In particular, the authors feel indebted to this referee for an idea about the origin of the irrotational dissipation that we explored in Appendix B. C.B.d.S. is supported by the Portuguese Minister of Science and Technology (MCTES) under ‘‘Ciência 2007.’’

## APPENDIX A: RESOLUTION TESTS

The present work analyzes quantities associated with extremely small and thus very intermittent scales of motion such as the invariants of the velocity gradient tensor  $Q$  and  $R$ . Therefore, it is useful to provide some additional resolution checks to the original DNS data bank. This is the purpose of this appendix. The kinetic energy and kinetic en-

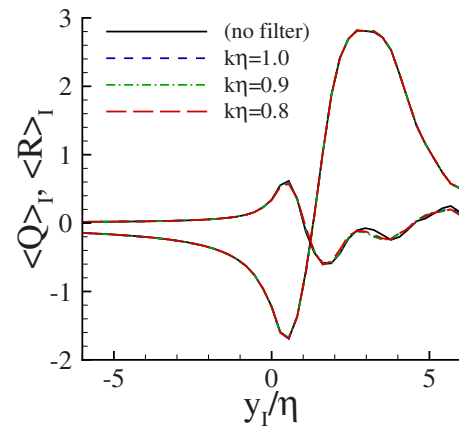


FIG. 18. (Color online) Conditional mean profiles of the invariants  $\langle Q\rangle_I$  and  $\langle R\rangle_I$  in the region  $-6 \leq y_I/\eta \leq 6$ , obtained after high pass filtering the DNS data, using a cutoff filter at  $k\eta=0.8, 0.9$ , and  $1.0$ . Results obtained without filtering (no filter) are also shown and the statistics were obtained using one single instantaneous field.

ergy dissipation spectra from the present DNS data were already discussed in Sec. II D with respect to Figs. 4(a) and 4(b), respectively. A referee suggested an additional test that we carry out here.

We start by defining three filter sizes:  $k\eta=0.8, 0.9$ , and  $1.0$ . Close inspection of Fig. 4(b) shows that these filters are placed well after the peak in dissipation, which is located at  $k\eta \approx 0.3$ . Therefore, if the present simulation is well resolved, high pass filtering of the DNS fields at  $k\eta=0.8, 0.9$ , and  $1.0$  will not cause any significant changes to the results.

Figure 18 shows the mean conditional profiles of the invariants  $\langle Q\rangle_I$  and  $\langle R\rangle_I$  in the region  $-6 \leq y_I/\eta \leq 6$ , where the DNS data was high pass filtered before the invariants were computed by using a cutoff filter at  $k\eta=0.8, 0.9$ , and  $1.0$ , respectively. Results without the application of any filter (‘‘no filter’’) are also shown for comparison. Here, in contrast to Fig. 15, only one single instantaneous field was used to compute the statistics. As can be seen, no significant difference can be observed between the four conditional mean profiles.

Figures 19(a) and 19(b) show the PDFs of  $Q$  and  $R$ , respectively, obtained without filtering the DNS data and by high pass filtering the data at  $k\eta=0.8, 0.9$ , and  $1.0$  prior to the computation of the invariants. The PDFs are nondimensionalized by the root mean square of the respective variable, e.g.,  $Q' = \langle Q'^2 \rangle^{1/2}$  in order to highlight the tails of the PDFs. The shape of the PDFs for the three cases are virtually equal for almost all their values. The zoom of the tails of the PDFs shows that only for PDF values below about  $1 \times 10^{-6}$  can we start discerning some (small) differences between the four cases, which shows that the differences between the results obtained with and without filtering are indeed very small. Thus, we conclude that the invariants are indeed well captured in the present simulation.

## APPENDIX B: THE ORIGIN OF THE VISCOUS DISSIPATION IN THE IRRATIONAL REGION

In this appendix, we analyze a pertinent question raised by a referee: Is the viscous dissipation found inside the irrotational (NT) flow region induced by instantaneous values of

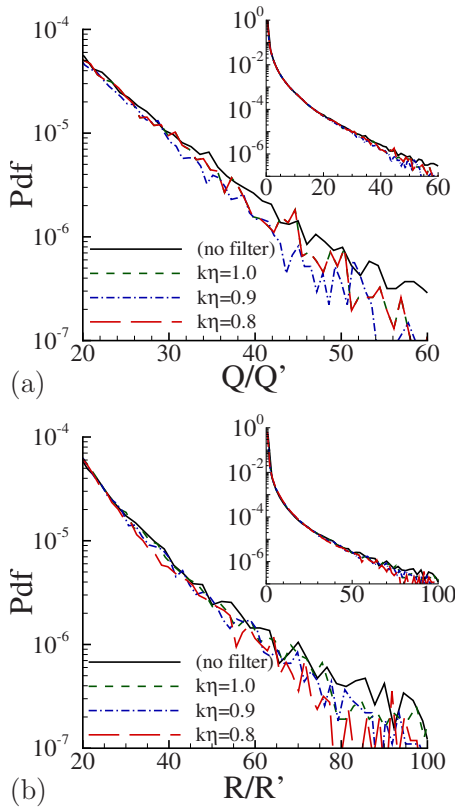


FIG. 19. (Color online) Joint PDFs of  $R$  and  $Q$  obtained after high pass filtering the DNS data with a cutoff filter at  $k\eta=0.8, 0.9$ , and  $1.0$ . Results obtained without filtering (no filter) are also shown.

pure shear caused by nearby large scale engulfing/entraining motions, or is it caused by incoherent irrotational velocity fluctuations near the T/NT interface?

If the dissipation is caused by small velocity fluctuations, then we expect them to be mainly associated with small scale motions, maybe with velocity and length scales characteristic of the nibbling motions associated with the entrainment mechanism. In this case, we expect them to be near isotropic due to the well known tendency to isotropy of small scale motions in turbulent flows. These small scale motions could be, for instance, originated by nonlocal effects caused by the fluctuating pressure field in the nearby turbulent region.

However, if the dissipation is caused by nearby large scale engulfing motions, we expect it to be associated with anisotropic velocity fluctuations since it seems plausible for the most frequent and the most intense of these entraining motions to be caused by the larger scale flow vortices in the jet, which are anisotropic and originate in the initial jet instabilities arising from the inlet (or initial) highest mean shear in the jet.

In order to investigate this problem, we decomposed the strain product  $S_{ij}S_{ij}$  into its six components,

$$S_{ij}S_{ij} = S_{11}^2 + S_{22}^2 + S_{33}^2 + 2S_{12}^2 + 2S_{13}^2 + 2S_{23}^2. \quad (\text{B1})$$

In isotropic turbulence, we have the following relations:<sup>45</sup>

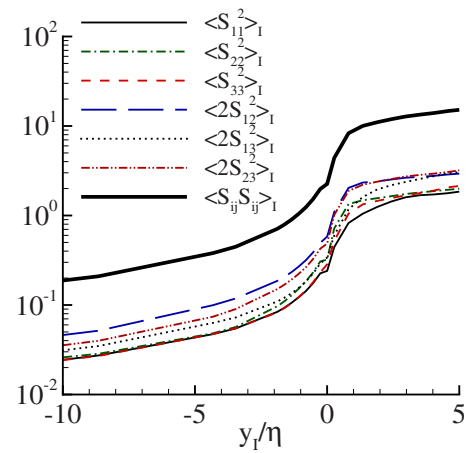


FIG. 20. (Color online) Conditional mean profiles of the six strain product terms defined in Eq. (B1) nondimensionalized by  $(U_1/H)^2$  near the T/NT interface. For simplicity, these conditional mean profiles were made using (only) 20 coordinate points in  $-10 \leq y_I/\eta \leq 5$ , while the other conditional mean profiles used in this work (e.g., in Fig. 10) use about 60 points in the same interval.

$$\left\langle \left( \frac{\partial u}{\partial x} \right)^2 \right\rangle = \left\langle \left( \frac{\partial v}{\partial y} \right)^2 \right\rangle = \left\langle \left( \frac{\partial w}{\partial z} \right)^2 \right\rangle, \quad (\text{B2})$$

$$\left\langle \left( \frac{\partial u_i}{\partial x_j} \right)^2 \right\rangle = 2 \left\langle \left( \frac{\partial u_i}{\partial x_i} \right)^2 \right\rangle \quad (\text{no summation}), \quad (\text{B3})$$

$$\left\langle \left( \frac{\partial u_i}{\partial x_j} \right) \left( \frac{\partial u_j}{\partial x_i} \right) \right\rangle = -\frac{1}{2} \left\langle \left( \frac{\partial u_i}{\partial x_i} \right)^2 \right\rangle \quad (\text{no summation}), \quad (\text{B4})$$

implying that  $\langle S_{11}^2 \rangle = \langle S_{22}^2 \rangle = \langle S_{33}^2 \rangle$ ,  $\langle S_{12}^2 \rangle = \langle S_{13}^2 \rangle = \langle S_{23}^2 \rangle$ , and  $\langle 2S_{12}^2 \rangle = \frac{3}{2} \langle S_{11}^2 \rangle$ .

Figure 20(a) shows the conditional mean profiles of the six terms defined in Eq. (B1) in the region  $-10 \leq y_I/\eta \leq 5$ , where  $i, j=1, 2$ , and  $3$  represent the  $x, y$ , and  $z$  directions, respectively. We start by analyzing the results from the turbulent region at  $y_I/\eta=4$ , where we have  $\langle S_{11}^2 \rangle_I \approx \langle S_{22}^2 \rangle_I \approx \langle S_{33}^2 \rangle_I \approx 1.8(U_1/H)^2$  and  $\langle 2S_{12}^2 \rangle_I \approx \langle 2S_{13}^2 \rangle_I \approx \langle 2S_{23}^2 \rangle_I \approx 2.8(U_1/H)^2$ . By using these conditional mean values, we obtain  $\langle 2S_{12}^2 \rangle_I / \langle S_{11}^2 \rangle_I = 2.8/1.8 \approx 1.55$ , i.e., very close to the isotropic value of  $\frac{3}{2}$ , which again confirms that the plane jet is (statistically) very nearly isotropic inside the turbulent region.

On the other hand, in the irrotational region at  $y_I/\eta=-4$ , we have  $\langle S_{11}^2 \rangle_I \approx \langle S_{22}^2 \rangle_I \approx \langle S_{33}^2 \rangle_I \approx 0.05(U_1/H)^2$ ,  $\langle 2S_{12}^2 \rangle_I \approx 0.1(U_1/H)^2$ ,  $\langle 2S_{13}^2 \rangle_I \approx 0.06(U_1/H)^2$ , and  $\langle 2S_{23}^2 \rangle_I \approx 0.075(U_1/H)^2$ , which give  $\langle 2S_{12}^2 \rangle_I / \langle S_{11}^2 \rangle_I \approx 2.0$ ,  $\langle 2S_{13}^2 \rangle_I / \langle S_{11}^2 \rangle_I \approx 1.2$ , and  $\langle 2S_{23}^2 \rangle_I / \langle S_{11}^2 \rangle_I \approx 1.5$ .

Although not very far from isotropic, these values are inconsistent with isotropic velocity fluctuations inside the NT region near the T/NT interface. Moreover, notice that the terms with the highest conditional mean, i.e.,  $\langle 2S_{12}^2 \rangle_I$  and  $\langle 2S_{23}^2 \rangle_I$ , are precisely the ones associated with  $\partial/\partial y$ , i.e., the direction of the highest mean shear in a plane jet. Thus, the present results seem to give support to the suggestion made by an anonymous referee in that the existence of a non-

negligible viscous dissipation outside the turbulent region is caused by instantaneous (local) pure shear motions induced by the large scale entraining motions.

However, in rigor, the present results do not really exclude the other possibility, i.e., nothing in the present results contradicts the possibility that both processes may exist, i.e., the irrotational dissipation may be caused both by instantaneous pure shear motions and by another small scale process. Clearly, this issue needs further study and should be addressed in future works.

- <sup>1</sup>M. Chong, E. Perry, and B. Cantwell, "A general classification of three-dimensional flow fields simulations of turbulence," *Phys. Fluids A* **2**, 765 (1990).
- <sup>2</sup>B. Cantwell, "Exact evolution of a restricted Euler equation for the velocity gradient tensor," *Phys. Fluids A* **4**, 782 (1992).
- <sup>3</sup>B. Cantwell, "On the behavior of velocity gradient tensor invariants in direct numerical simulations of turbulence," *Phys. Fluids A* **5**, 2008 (1993).
- <sup>4</sup>A. Perry and M. Chong, "Topology of flow patterns in vortex motions and turbulence," *Appl. Sci. Res.* **53**, 357 (1994).
- <sup>5</sup>J. Martín, A. Ooi, S. Chong, and J. Soria, "Dynamics of the velocity gradient tensor invariants in isotropic turbulence," *Phys. Fluids* **10**, 2336 (1998).
- <sup>6</sup>K. Nomura and G. Post, "The structure and dynamics of vorticity and rate of strain in incompressible homogeneous turbulence," *J. Fluid Mech.* **377**, 65 (1998).
- <sup>7</sup>A. Ooi, J. Martín, J. Soria, and M. Chong, "A study of the evolution and characteristics of the invariants of the velocity-gradient tensor in isotropic turbulence," *J. Fluid Mech.* **381**, 141 (1999).
- <sup>8</sup>J. Soria, R. Sondergaard, B. Cantwell, M. Chong, and A. Perry, "A study of the fine-scale motions of incompressible time-developing mixing layers," *Phys. Fluids* **6**, 871 (1994).
- <sup>9</sup>H. Blackburn, N. Mansour, and B. Cantwell, "Topology of fine-scale motions in turbulent channel flow," *J. Fluid Mech.* **310**, 269 (1996).
- <sup>10</sup>J. Soria, A. Ooi, and M. Chong, "Volume integrals of the  $Q_A - R_A$  invariants of the velocity gradient tensor in incompressible flows," *Fluid Dyn. Res.* **19**, 219 (1997).
- <sup>11</sup>P. Vieillefosse, "Internal motion of a small element of fluid in an inviscid flow," *Physica A* **125**, 150 (1984).
- <sup>12</sup>W. Ashurst, A. Kerstein, R. Kerr, and C. Gibson, "Alignment of vorticity and scalar gradient with strain rate in simulated Navier-Stokes turbulence," *Phys. Fluids* **30**, 2343 (1987).
- <sup>13</sup>J. Weiss, *The Dynamics of Enstrophy Transfer in Two-Dimensional Hydrodynamics* (La Jolla Institute, San Diego, CA, 1981).
- <sup>14</sup>J. C. R. Hunt, A. A. Wray, and P. Moin, *Annual Research Briefs* (Center for Turbulence Research, Stanford, 1988).
- <sup>15</sup>I. Dubief and F. Delcayre, "On coherent-vortex identification in turbulence," *J. Turbul.* **1**, 11 (2000).
- <sup>16</sup>J. Soria and B. Cantwell, "Topological visualisation of focal structures in free shear flows," *Appl. Sci. Res.* **53**, 375 (1994).
- <sup>17</sup>K. Horiuti, "A classification method for vortex sheet and tube structures in turbulent flows," *Phys. Fluids* **13**, 3756 (2001).
- <sup>18</sup>K. Horiuti and Y. Takagi, "Identification method for vortex sheet structures in turbulent flows," *Phys. Fluids* **17**, 121703 (2005).
- <sup>19</sup>F. van der Bos, B. Tao, C. Meneveau, and J. Katz, "Effects of small-scale turbulent motions on the filtered velocity gradient tensor as deduced from holographic particle image velocimetry measurements," *Phys. Fluids* **14**, 2456 (2002).
- <sup>20</sup>B. Wang, D. Bergstrom, J. Yin, and E. Yee, "Turbulence topologies predicted using large eddy simulations," *J. Turbul.* **7**, 34 (2006).
- <sup>21</sup>S. Corrsin and A. L. Kistler, "Free-stream boundaries of turbulent flows," NACA Technical Report No. TN-1244, 1955.
- <sup>22</sup>J. C. R. Hunt, I. Eames, and J. Westerweel, "Mechanics of inhomogeneous turbulence and interfacial layers," *J. Fluid Mech.* **554**, 499 (2006).
- <sup>23</sup>A. A. Townsend, *The Structure of Turbulent Shear Flow* (Cambridge University Press, Cambridge, 1976).
- <sup>24</sup>J. S. Turner, "Turbulent entrainment: The development of the entrainment assumption, and its application to geophysical flows," *J. Fluid Mech.* **173**, 431 (1986).
- <sup>25</sup>J. Mathew and A. Basu, "Some characteristics of entrainment at a cylindrical turbulent boundary," *Phys. Fluids* **14**, 2065 (2002).
- <sup>26</sup>J. Westerweel, C. Fukushima, J. M. Pedersen, and J. C. R. Hunt, "Mechanics of the turbulent-nonturbulent interface of a jet," *Phys. Rev. Lett.* **95**, 174501 (2005).
- <sup>27</sup>D. K. Bisset, J. C. R. Hunt, X. Cai, and M. M. Rogers, *Annual Research Briefs* (CTR, Stanford, 1998).
- <sup>28</sup>D. K. Bisset, J. C. R. Hunt, and M. M. Rogers, "The turbulent/nonturbulent interface bounding a far wake," *J. Fluid Mech.* **451**, 383 (2002).
- <sup>29</sup>J. Westerweel, T. Hofmann, C. Fukushima, and J. C. R. Hunt, "The turbulent/non-turbulent interface at the outer boundary of a self-similar turbulent jet," *Exp. Fluids* **33**, 873 (2002).
- <sup>30</sup>M. Holzner, A. Liberzon, M. Guala, A. Tsinober, and W. Kinzelbach, "Generalized detection of a turbulent front generated by an oscillating grid," *Exp. Fluids* **41**, 711 (2006).
- <sup>31</sup>M. Holzner, A. Liberzon, N. Nikitin, W. Kinzelbach, and A. Tsinober, "Small-scale aspects of flows in proximity of the turbulent/nonturbulent interface," *Phys. Fluids* **19**, 071702 (2007).
- <sup>32</sup>W. C. Reynolds, "Large-scale instabilities of turbulent wakes," *J. Fluid Mech.* **54**, 481 (1972).
- <sup>33</sup>S. Stanley, S. Sarkar, and J. P. Mellado, "A study of the flowfield evolution and mixing in a planar turbulent jet using direct numerical simulation," *J. Fluid Mech.* **450**, 377 (2002).
- <sup>34</sup>C. B. da Silva and O. Métais, "On the influence of coherent structures upon interscale interactions in turbulent plane jets," *J. Fluid Mech.* **473**, 103 (2002).
- <sup>35</sup>R. Akhavan, A. Ansari, S. Kang, and N. Mangiavacchi, "Subgrid-scale interactions in a numerically simulated planar turbulent jet and implications for modelling," *J. Fluid Mech.* **408**, 83 (2000).
- <sup>36</sup>C. B. da Silva and J. C. F. Pereira, "The effect of subgrid-scale models on the vortices obtained from large-eddy simulations," *Phys. Fluids* **16**, 4506 (2004).
- <sup>37</sup>F. O. Thomas and H. C. Chu, "An experimental investigation of the transition of the planar jet: Subharmonic suppression and upstream feedback," *Phys. Fluids A* **1**, 1566 (1989).
- <sup>38</sup>A. Basu and R. Narashima, "Direct numerical simulation of turbulent flows with cloud-like off-source heating," *J. Fluid Mech.* **385**, 199 (1999).
- <sup>39</sup>C. Canuto, M. Y. Hussaini, A. Quarteroni, and T. A. Zang, *Spectral Methods in Fluid Dynamics* (Springer-Verlag, Berlin, 1987).
- <sup>40</sup>J. H. Williamson, "Low-storage Runge-Kutta schemes," *J. Comput. Phys.* **35**, 48 (1980).
- <sup>41</sup>C. B. da Silva and O. Métais, "Vortex control of bifurcating jets: A numerical study," *Phys. Fluids* **14**, 3798 (2002).
- <sup>42</sup>P. Freymuth, "On transition in a separated laminar boundary layer," *J. Fluid Mech.* **25**, 683 (1966).
- <sup>43</sup>M. Lesieur, S. Ossia, and O. Métais, "Infrared pressure spectra in 3D and 2D isotropic incompressible turbulence," *Phys. Fluids* **11**, 1535 (1999).
- <sup>44</sup>S. Stanley and S. Sarkar, "Influence of nozzle conditions and discrete forcing on turbulent planar jets," *AIAA J.* **38**, 1615 (2000).
- <sup>45</sup>S. B. Pope, *Turbulent Flows* (Cambridge University Press, Cambridge, 2000).
- <sup>46</sup>Note that the initial Reynolds number used in Ref. 36 was in fact 3000 and not 1500 as was by mistake written in that article.
- <sup>47</sup>P. A. Monkewitz and P. Huerre, "Influence of the velocity ratio on the spatial instability of mixing," *Phys. Fluids* **25**, 1137 (1982).
- <sup>48</sup>B. Vreman, B. Geurts, and H. Kuerten, "Large eddy simulation of the turbulent mixing layer," *J. Fluid Mech.* **339**, 357 (1997).
- <sup>49</sup>S. Ghosal and M. Rogers, "A numerical study of self-similarity in a turbulent plane wake using large-eddy simulation," *Phys. Fluids* **9**, 1729 (1997).
- <sup>50</sup>E. Gutmark and I. Wygnansky, "The planar turbulent jet," *J. Fluid Mech.* **73**, 465 (1976).
- <sup>51</sup>R. Ramparion and M. S. Chandrasekhara, "LDA measurements in plane turbulent jets," *ASME J. Fluids Eng.* **107**, 264 (1985).
- <sup>52</sup>F. O. Thomas and K. M. K. Prakash, "An investigation of the natural transition of an untuned planar jet," *Phys. Fluids A* **3**, 90 (1991).
- <sup>53</sup>P. A. Davidson, *Turbulence, An Introduction for Scientists and Engineers* (Oxford University Press, New York, 2004).
- <sup>54</sup>J. Jimenez, A. Wray, P. Saffman, and R. Rogallo, "The structure of intense vorticity in isotropic turbulence," *J. Fluid Mech.* **255**, 65 (1993).
- <sup>55</sup>E. Balaras, U. Piomelli, and J. Wallace, "Self-similar states in turbulent mixing layers," *J. Fluid Mech.* **446**, 1 (2001).
- <sup>56</sup>F. Moisy and J. Jiménez, "Geometry and clustering of intense structures in isotropic turbulence," *J. Fluid Mech.* **513**, 111 (2004).